nature communications



Article

https://doi.org/10.1038/s41467-025-57938-9

The impact of a high fat diet and platelet activation on pre-metastatic niche formation

Received: 5 August 2024

Accepted: 7 March 2025

Published online: 02 April 2025



Marta Hergueta-Redondo¹, Sara Sánchez-Redondo¹, Begoña Hurtado $\textcircled{0}^2$, Vanesa Santos¹, Manuel Pérez-Martínez $\textcircled{0}^3$, Pilar Ximénez- Embún⁴, Sheri A. C. McDowell⁵, Marina S. Mazariegos^{1,6,7}, Gadea Mata $\textcircled{0}^{3,8}$, Raúl Torres-Ruiz $\textcircled{0}^{9,10,11,12}$, Sandra Rodríguez-Perales $\textcircled{0}^9$, Lola Martínez¹³, Osvaldo Graña-Castro $\textcircled{0}^{14,15}$, Diego Megias^{3,16}, Daniela Quail $\textcircled{0}^5$, Miguel Quintela-Fandino $\textcircled{0}^{17,18}$ & Héctor Peinado $\textcircled{0}^1$

There is active crosstalk between tumor cells and the tumor microenvironment during metastatic progression, a process that is significantly affected by obesity, particularly in breast cancer. Here we analyze the impact of a high fat diet (HFD) on metastasis, focusing on the role of platelets in the formation of premetastatic niches (PMNs). We find that a HFD provokes pre-activation of platelets and endothelial cells, promoting the formation of PMNs in the lung. These niches are characterized by increased vascular leakiness, platelet activation and overexpression of fibronectin in both platelets and endothelial cells. A HFD promotes interactions between platelets, tumor cells and endothelial cells within PMNs, enhancing tumor cell homing and metastasis. Importantly, therapeutic interventions like anti-platelet antibody administration or a dietary switch reduce metastatic cell homing and outgrowth. Moreover, blocking fibronectin reduces the interaction of tumor cells with endothelial cells. Importantly, when coagulation parameters prior to neoadjuvant treatment are considered, triple negative breast cancer (TNBC) female patients with reduced Partial Thromboplastin time (aPTT) had a significantly shorter time to relapse. These findings highlight how diet and platelet activation in pre-metastatic niches affect tumor cell homing and metastasis, suggesting potential therapeutic interventions and prognostic markers for TNBC patients.

Metastasis is a complex process in which cancer cells must adapt to the diverse microenvironments they encounter as they disseminate to distant tissues^{1,2}. In recent decades, it has become clear that tumor cell metastasis depends both on intrinsic alterations to tumor cells and extrinsic effects of the tumor microenvironment (TME)³. For example, it is known that obesity contributes to the progression of several cancer types, including endometrial, ovarian, pancreatic, colon and breast cancers (BCs)^{4,5}. In addition, obesity is correlated to poor outcomes of BC in postmenopausal women⁶ and in triple-negative breast

cancer (TNBC) patients⁷. As well as affecting primary BC tumor growth, obesity enhances the metastasis of these cells to the lungs in a manner that is dependent on neutrophils^{8,9}, involving vascular dysfunction and increased endothelial transmigration of the tumor cells¹⁰. Moreover, obesity also induces chronic inflammation, while enhancing prothrombotic signaling in both platelets and endothelial cells^{11,12}, and promoting a state of hypercoagulability in cancer patients¹³. Notably, exacerbated coagulation is related to worse patient survival in a variety of tumor types, underscoring the pro-metastatic role of platelets¹⁴.

A full list of affiliations appears at the end of the paper. e-mail: hpeinado@cnio.es

Platelets have been implicated in tumor progression through several mechanisms, as they can interact with different cell types like leukocytes, or stromal, endothelial and cancer cells^{15,16}. Indeed, platelets surrounding circulating tumor cells play an important role in tumor cell survival and metastasis, impeding their recognition by immune cells^{17–19}. Hence, defining the precise mechanisms involved in the tumor-platelet-endothelial cell interactions is of particular interest. Platelets have also been implicated in the early metastatic dissemination of colon cancer and melanoma^{20,21}. Upon activation, platelets release growth factors, cytokines and extracellular vesicles that help remodel the extracellular matrix (ECM) and that are involved in the recruitment of other cells to the metastatic organs^{20,21}. However, the precise influence of extrinsic factors like a high fat diet (HFD) on platelet activation and the formation of pre-metastatic niches (PMNs)²² remains unclear and warrants further investigation.

Here we show that a HFD promotes the generation of PMNs in distal organs, aiding metastatic cell homing. Our data demonstrate that a HFD contributes to platelet activation, and that it enhances vascular permeability and fibronectin (FN) overexpression in the lungs. Moreover, we find that adipose tissue in HFD-fed mice secretes high levels of TNF-α, which leads to increased FN levels and its subsequent accumulation in platelets. Notably, platelets from HFD-fed mice exhibit greater interactions with tumor cells within PMNs, reinforcing the tumor-endothelial-platelet cell axis. Furthermore, a HFD exacerbates tumor cell homing and metastasis, yet only in highly-metastatic BC models, suggesting that both intrinsic and extrinsic factors are crucial for metastatic success. Our results suggest that therapeutic interventions, such as anti-platelet antibody administration or dietary modifications, reduce metastatic cell homing and outgrowth, underscoring the potential of dietary and platelet-modulating strategies in influencing disease outcomes. Additionally, blocking FN reduces plateletmediated interactions between tumor cells and endothelial cells, highlighting its pivotal role in this process. Finally, in triple-negative breast cancer (TNBC) patients, we observe a correlation between the body mass index (BMI) and higher pro-coagulant activity. Patients with a shorter activated Partial Thromboplastin time (aPTT) show increased risk and lower survival rates over three years post-treatment, suggesting a short aPTT as a risk factor in TNBC prior to surgery. Collectively, our findings reveal the impact of HFD on platelet activation, PMN formation, and metastasis in TNBC, offering potential therapeutic targets and prognostic markers for cancer management.

Results

A HFD enhances platelet activation and aggregation

In this study, a diet-induced obesity (DIO) model was chosen to assess how a HFD might affect PMN formation in pre-metastatic lungs (Suppl. Figure 1A), initially verifying that the HFD produced a weight gain in these mice over the 12week study period (Suppl. Figure 1B-E). The impact of the HFD on platelet activation was assessed and since platelet activation results in dense granule secretion and a conformational change of integrin $\alpha_{IIb}\beta_3^{\ 23,24}$, these parameters were analyzed in mice by flow cytometry using anti-GPIIb/IIIa (JON/A) and anti-P-selectin (CD62P) antibodies (Fig. 1A). Interestingly, the platelets from HFD mice were more susceptible to activation by exposure to thrombin for 5 or 15 minutes relative to those from ND mice (Fig. 1A, B). In terms of dense granule secretion in response to thrombin stimulation, ATP luminometry revealed a significant increase in such release by platelets from HFD mice relative to those from ND mice (Fig. 1C). Since fibrinogen (Fg) binding to platelets promotes their spreading, an important step in the amplification process²⁵, we analyzed this phenomenon in mice. Enhanced Fg adhesion was evident in platelets from HFD mice (Fig. 1D), coupled to significantly accelerated spreading (Fig. 1E-G). There was a particular enrichment in the filopodial (Fp, red bars, Fig. 1G) and spread phenotypes (Sp, green bars, Fig. 1G), for which cytoskeletal reorganization is crucial. Moreover, the HFD exacerbated platelet aggregation (Fig. 1 H), demonstrating that a HFD promotes both platelet activation and aggregation.

To gain further insights into the mechanisms driving platelet activation and aggregation in response to thrombin, signaling activation in platelets from ND and HFD mice was analyzed at different time points after treatment (Fig. 1I–M, Suppl. Figures 1F–J). Platelets from HFD mice displayed sustained Src phosphorylation (Fig. 1I, Suppl. Figure 1F), which is essential to initiate and propagate signals from $\alpha \text{Ilb}\beta 3$ through the "inside-out" signaling pathway²6,27. A similar effect was observed on protein kinase C (PKC: Fig. 1J, Suppl. Figure 1G), which has been shown to play a major role in inducing platelet granule secretion²8,29. Moreover, at later times there was enhanced AKT phosphorylation ((Fig. 1K, Suppl. Figure 1H), previously implicated in α -granule secretion³0), FAK (Fig. 1L, Suppl. Figure 1I) and Talin (Fig. 1M, Suppl. Figure 1J), both Src substrates involved in cell adhesion and cytoskeletal reorganization in platelets³1.

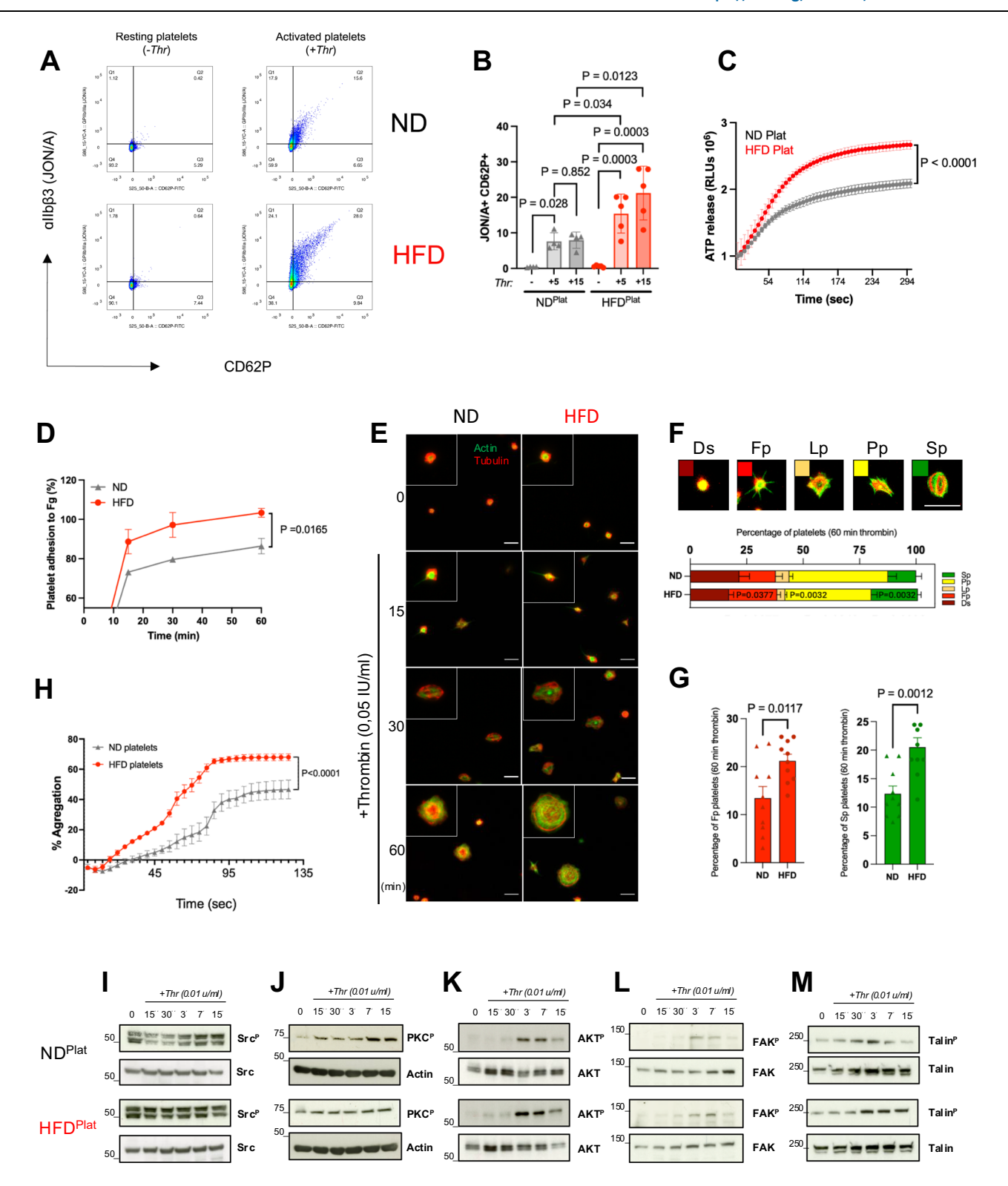
In the light of all these data, our results suggest that a HFD promotes the activation of integrin α IIb β 3 through the 'inside-out' signaling pathway, followed by 'outside-in' downstream signaling^{32,33} that leads to platelet activation, cytoskeletal reorganization and platelet spreading.

A HFD promotes vascular leakiness in the lung and fibronectin expression

Platelets have been implicated in early metastasis in mice²⁰, yet the impact of platelets and a HFD on PMN formation has been little explored. To assess the effect of HFD on PMN formation, platelet recruitment to the lungs of mice was analyzed. Interestingly, significantly enhanced P-selectin expression was evident in the lungs of HFD mice relative to the controls (Fig. 2A, B), showing a higher presence of platelets in the metastatic organs of HFD mice. Since obesityassociated inflammation is involved in endothelial cell disfunction³⁴, we also studied the impact of a HFD on lung endothelial cell leakiness. Vascular leakiness was assessed by injecting fluorescent dextran into HFD or ND mice, which underwent greater extravasation in the former (Fig. 2C. D). Whether this leakiness was due to high adiposity, or the diet itself was explored in ob/ob mice35,36. These ob/ob mice also exhibited significantly enhanced vascular permeability in the lungs relative to wild type (WT) mice (Suppl. Figures 2A, 2B), demonstrating the increase in vascular leakiness regardless of the model assessed.

We next explored the impact of the HFD on lung endothelial cells by analyzing gene expression in CD45⁻CD31⁺ lung endothelial cells isolated from the mice by RNA-sequencing (RNA-seq) (Suppl. Figure 2C, Suppl. Data 1). A gene set enrichment analysis (GSEA) identified signatures of enrichment related to the inflammatory response, cell adhesion and hemostasis, amongst other gene pathways (Suppl. Figure 2D, Suppl. Data 1). We found that three of the top ten pathways were enriched in genes related to cell adhesion (Jam2, Ocln, Dsp, Panx1), inflammatory responses (Ikbkb, Tlr3, Cmip) and hemostasis (Plaur, Plat, Fn1) (Suppl. Figure 2D, Table 1). To identify common pathways affected in both platelets and endothelial cells isolated from HFD mice we integrated the RNA expression data from endothelial cells and the proteomic analyzes of platelets-derived from mice fed with either diet (Fig. 2F). Out of 2916 candidate genes modulated, we identified 6 that were upregulated in both endothelial cells and platelets from HFD mice, with a FDR < 0.05 (Fig. 2F). Among these, fibronectin (FN) attracted our attention since it was previously associated with lung PMN formation³⁷.

Immunohistochemical staining revealed FN to be significantly overexpressed in the lungs of HFD mice (Fig. 2G, H). To determine the origin of this FN expression, the lungs of mice perfused intracardially with PBS and non-perfused lungs were analyzed in Western blots (Fig. 2I). A significantly enhanced FN expression was detected in non-perfused whole lung tissues (Fig. 2J), suggesting an increase in blood circulation. We next analyzed FN expression in plasma and platelets



isolated from the blood of ND and HFD mice (Fig. 2K, L) and while there were no differences in the FN in plasma (Fig. 2M), a significant increase in FN was evident in platelets reflecting its upregulation (Fig. 2N).

To assess the expression of FN in HFD-induced PMNs, we examined lung sections from our DIO model by confocal immuno-fluorescence microscopy (Suppl. Figure 2E). We analyzed FN co-expression with P-selectin (platelets) and CD31 (endothelial cells). We found that its expression was elevated in platelet aggregates (Suppl. Figure 2F), exhibiting a higher fluorescence intensity within the lungs of HFD mice (Suppl. Figure 2G). Conversely, there was negligible co-

expression in the lungs of ND mice and as expected, there were almost no platelet aggregates in the lungs of these mice (Suppl. Figure 2E), indicative of specific co-expression and deposition of FN in platelet aggregates (P-selectin⁺ areas) in HFD mice. Furthermore, there was only a marginal and non-significant increase in FN staining of endothelial cells (CD31⁺, Suppl. Figure 2H), demonstrating that platelets are the primary source of FN in the lungs of HFD mice reflecting their activation at PMNs.

Since thrombus formation has been proposed to facilitate fibrinogen and fibronectin internalization in other contexts³⁸, we **Fig. 1** | **A HFD enhances platelet activation and aggregation. A** Analysis of platelet activation by flow cytometry, measuring the expression of activated αIIbβ3 integrin and CD62P in both the presence (Activated platelets) and absence (Resting platelets) of thrombin (0.05 IU/ml). **B** Graph showing the quantification of the experiment shown in (**A**), at the times indicated. 5 independent experiments: ND n = 4, HFD n = 5 platelet samples per group. **C** Platelets from ND or HFD mice were incubated with the luciferase-luciferin reagent and ATP release was measured in a luminometer upon thrombin stimulation. 2 independent experiments: n = 3 platelet samples per group. **D** Quantitative analysis of the relative platelet adhesion to fibrinogen (%) over time. 4 independent experiments: n = 4 platelet samples per group. **E** Spreading of platelets on fibrinogen. Platelets were stained with α-tubulin (red) and phalloidin (green). Bar: 5 μm. **F** Quantification of platelet morphology after thrombin activation on fibrinogen for 60 minutes. Representative images of platelet morphology are shown: discoid (Ds), filopodial (Fp), pseudopodial (Pp),

lamellipodia (Lp), and spread (Sp). Bar: 5 μ m. The plot below indicates the proportion of cells in each category (>150 cells per experiment), showing the mean \pm SEM of each morphology. **G** Detail of the proportion of platelets with a Fp (red bars) and Sp morphology (green bars). 2 independent experiments: n=9 images per group. **H** Analysis of platelet aggregation in ND and HFD mice, assessing their response to thrombin (0.01 IU/ml). 3 independent experiments: ND n=9, HFD n=10 mice. I-M) Western blots of (I) phospho Src/Src, J phospho PKC/Actin, **K** phospho AKT/AKT, **L** phospho FAK/FAK and (**M**) phospho Talin/Talin in platelets isolated from ND (Upper panels) or HFD (Lower panels) mice, untreated (0) or activated with thrombin for the times indicated. The data corresponds to 3 independent experiments: ND n=9, and HFD n=10. All the data represent the mean \pm s.d. and the P values were calculated two-way ANOVA (**C**, **D**, **H**) or with a two-tailed Student's t-test (**B**. **G**).

investigated whether platelets from ND- and HFD-fed mice differ in their ability to bind and internalize FN. To do this, platelets isolated from both groups were incubated with FITC-FN and then fixed before and after the addition of trypan blue to distinguish between FN binding and internalization, respectively. Our results revealed that platelets from HFD-fed mice displayed a increassed capacity to both bind and internalize FN (Fig. 2O, P, Q) compared with those from ND-fed mice.

To identify potential factors involved in this mechanism, we analyzed the expression of cytokines in adipose tissue and platelets from HFD-fed mice compared to ND-fed mice. Our analysis revealed that several factors, including TNF- α , CCL3, Thrombopoietin, Angiopoietin-1, TIM-1, IL-22, Leptin, among others were significantly elevated in both conditions (Suppl. Figure 2I). Given the crucial role of TNF- α in obesity³⁹, we further investigated its effect on FN production by platelets. Interestingly, we observed that the treatment significantly increased FN levels in platelets, reaching levels comparable to those observed in platelets from HFD-fed mice (Suppl. Figure 2J, K).

A HFD enhances tumor cell homing and metastasis to the lung

To evaluate the impact of a HFD on spontaneous BC metastasis, EO771 cells were injected into the mammary fat pad of DIO mice and analyzed 22 days after injection. Primary tumor growth increased in the HFD mice (Fig. 3A) and when tumor cells were stained for p53⁴⁰, a 3.17-fold increase in lung metastasis was detected (Fig. 3B, C). Moreover, among these metastases 69.3% existed as individual cells (Fig. 3C). To mitigate the potential impact of variations in primary tumor size on spontaneous metastasis, we compared the metastases in mice with similar tumor sizes on day 14 (Fig. 3D) when there were 4.7-fold more metastases in the lung of HFD mice (Fig. 3E, F). Interestingly, among these metastases 64.9% were individual cells (Fig. 3F), suggesting that the HFD specifically enhanced tumor cell homing and early adhesion

To assess how a HFD influences tumor homing, EO771-GFP-luciferase cells were injected into the tail vein of ND and HFD mice and mice were sacrificed after one hour (See Fig. 3G for a scheme of tumor cell homing assays). Remarkably, the HFD significantly enhanced tumor cell homing to the lungs (Fig. 3H-I). These findings were consistent when three additional murine BC models were assessed (Py230-Luc, Py8119-Luc and AT3-Luc: Suppl. Figure 3A–C). Tumor cell homing was also analyzed in *ob/ob* mice to determine whether this effect was influenced by high adiposity or the diet, and as no significant differences in tumor cell homing were observed in the lungs (Suppl. Figure 3D), it appears that this phenomenon is only affected by the HFD.

The impact of HFD on tumor cell metastasis was further investigated in the highly metastatic EO771 model, analyzing lung metastasis at early (12 days post injection –p.i.) and late (3 weeks p.i.) time points. The HFD enhanced metastasis at the early time point (Fig. 3J, Supp. Figure 3E), when the metastases were predominantly detected as single cells (2.2-fold change), followed by small metastases (2.8-fold change), micrometastases (1.5-fold change) and macrometastases (1.5-

fold change: Fig. 3K). This effect was particularly prominent at the later time points (Suppl. Figure 3F–H). Similarly, with the Py8119-luc model an 11-fold increase in experimental metastasis was evident in the lungs of HFD compared to ND mice (Suppl. Figure 3I). By contrast, the HFD did not increase metastasis when the low metastatic AT3 model was assessed (Suppl. Figure 3J), suggesting that both intrinsic and extrinsic changes influence metastatic spread.

A HFD reinforces the tumor-platelet-endothelial cell interaction

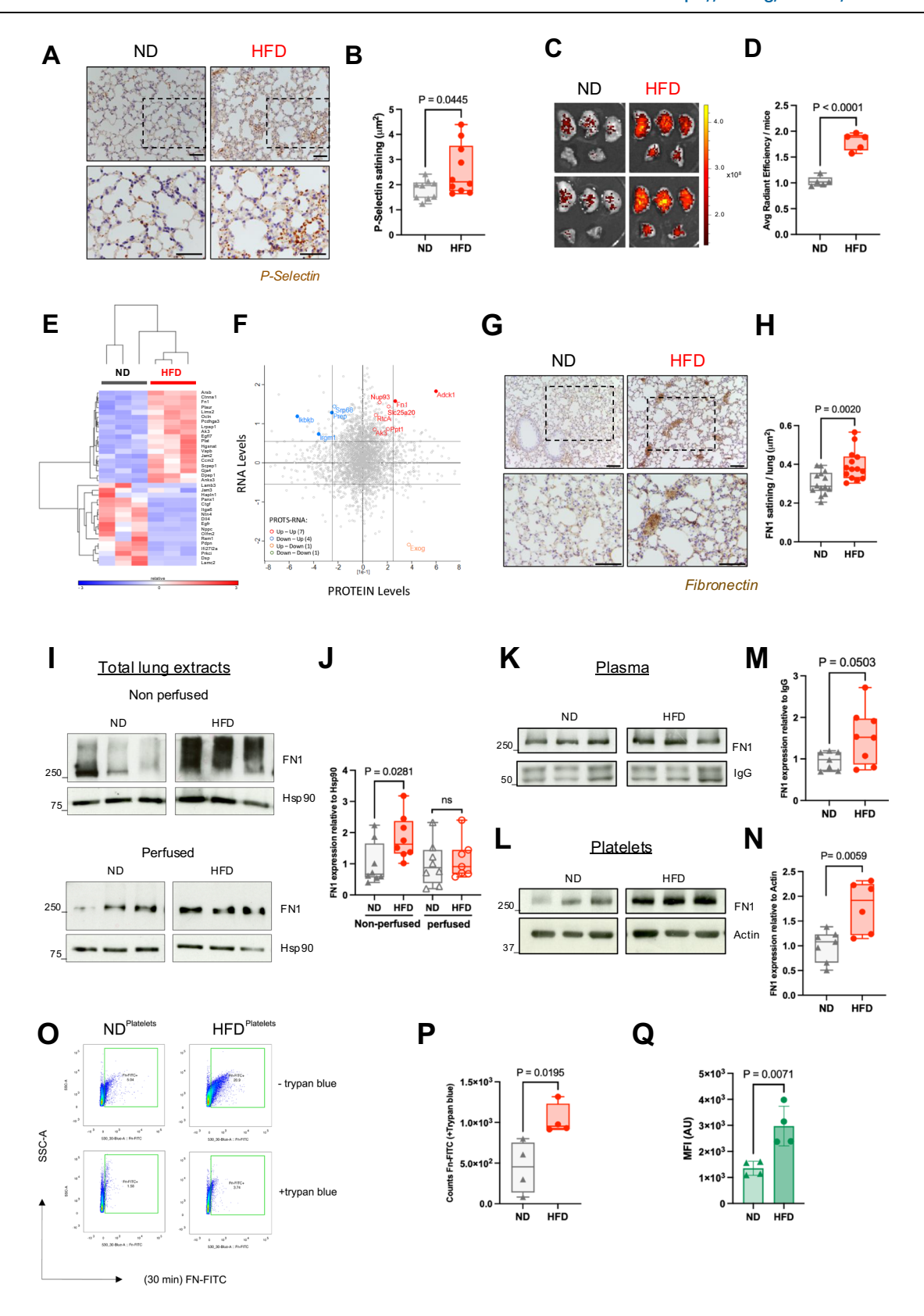
The pro-metastatic effects of platelets have traditionally been attributed to their ability to promote tumor cell adhesion or survival²¹, leading us to study the influence of a HFD on platelet and tumor cell interactions with endothelial cells. Platelets derived from HFD models adhered more to EO771 tumor cells than platelets derived from ND mice (Fig. 4A, B), as they also did to the low metastatic model AT3 cells (Suppl. Figure 4A, B). We next examined whether platelets from HFD-fed and ND-fed mice differ in their shape upon contact with tumor cells, as platelet morphology provides valuable insights into their activation potential. Our findings revealed that activated platelets from HFD-fed mice displayed an increased number of aggregating platelets, characterized by numerous membrane extensions and the formation of larger aggregates as demonstrated by scanning electron microscopy (Fig. 4C, D).

To determine if the enhanced tumor-platelet interaction also influences their interaction with endothelial cells, tumor-platelet-endothelial interactions were assayed in chambers coated with a monolayer of HUVECs (Human Umbilical Vein Endothelial Cells: Fig. 4E). Platelets from HFD mice adhered more to endothelial cells (Fig. 4F) and tumor cells (Fig. 4G), and interestingly, transwell transendothelial migration (TEM) assays revealed that platelets from obese mice migrated more efficiently than those from lean mice when injected with Py230 or EO771 cells (Suppl. Figure 4C).

To study the effect of a HFD on platelet-tumor interactions in vivo, high-resolution intravital imaging of EO771GFP tumor cells injected into the tail vein was carried out on the lung of HFD or ND mice. The area covered by platelets surrounding the tumor cells was measured in vivo (see Suppl. Figure 4D–E for a scheme), indicating that platelets were recruited around tumor cells in the lungs of mice as early as 1 minute after tumor cell injection in both ND and HFD mice (Suppl. Figure 4F–G and Video 1). Tumor-platelet aggregation 30 minutes after injection reflected how platelets from HFD mice interacted more efficiently with tumor cells in PMNs than those from ND mice (Fig. 4H–I).

Platelets from HFD-fed mice activate endothelial cells more efficiently

The enhanced FN expression by platelets and endothelial cells induced by a HFD suggests that FN might modulate tumor-endothelial-platelet interactions. Hence, FN expression by endothelial cells exposed to platelets from ND and HFD mice was assessed by immunofluorescence, with FN and CD41 staining highlighting the upregulation



of FN expression (Fig. 4J, green channel) and the enhanced interaction of platelets from HFD mice with endothelial cells (Fig. 4J, red channel). Platelets from HFD mice induced stronger FN expression in fibers surrounding endothelial cells (Fig. 4J panel inset, lower panels), whereas no fibers were observed with platelets from ND mice, when FN was poorly organized (Fig. 4J panel inset, upper panels) a significant

increase in cortical FN was evident in endothelial cells treated with platelets from HFD mice relative to those from ND mice (Fig. 4K).

Since FN is known to be involved in intracellular signaling in endothelial cells^{41–43}, we assessed the activity of the main downstream pathways implicated in regulating cell adhesion, cytoskeletal reorganization and endothelial permeability, through the effectors Src and

Fig. 2 | A HFD promotes vascular leakiness and fibronectin expression.

A Representative images of P-Selectin staining in the lungs of ND and HFD-fed mice. Bottom panels are magnifications of the boxed area. Bar: 50 μ m (**B**) Quantitative analysis of P-Selectin staining in the lungs of ND and HFD mice. 2 independent experiments: ND n=9 fields, HFD n=10 fields per group. **C** Representative images of the vascular permeability in the lungs of ND and HFD mice visualized with NIR-Dextran. **D** Quantification of (**C**). 3 independent experiments: n=11 mice per group. **E** Heatmap of genes in endothelial cells from ND and HFD mice based on RNA-seq data: n=3 mice per group. **F** Correlation between the RNA-seq data and the proteomic data from ND and HFD mice (FDR < 0.05) and fold change.

G Representative images of FNI staining in the lungs of ND and HFD mice. Bottom panels are magnifications of the boxed area. Bar: $100 \mu m$. **H** Quantification of **G**. 2 independent experiments: n = 14 fields per group. **I** Representative Western blot of

FNI in whole lung extracts comparing non-perfused and perfused lungs from both ND and HFD mice. **J** Quantification of the experiments in **I**. Data correspond to 2 independent experiments ND (n = 8 perfused and n = 8 non-perfused) and HFD (n = 8 perfused and n = 7 non-perfused). Representative Western blot of FNI in plasma (**K**) and platelets (**L**) isolated from ND and HFD mice. **M**, **N** Quantification of the experiments in K and L respectively. 2 independent experiments, M (ND n = 7, HFD n = 8), N (ND n = 7, HFD n = 6) platelet samples per group. **Q**) Analysis of platelet fibronectin uptake by flow cytometry expressed as total counts (**P**) or MFI (**Q**). The data corresponds to 4 independent experiments: n = 3 platelet samples per group. All the data represent the mean \pm s.d., and the P values were calculated with a two-tailed Student's t-test (**B**, **D**, **H**, **M**, **N**, **P**, **Q**) or Mann-Whitney test (**J**). Values are shown in box-and-whisker plots where the line in the box corresponds to the mean. Boxes extend from the minimum to the maximum value.

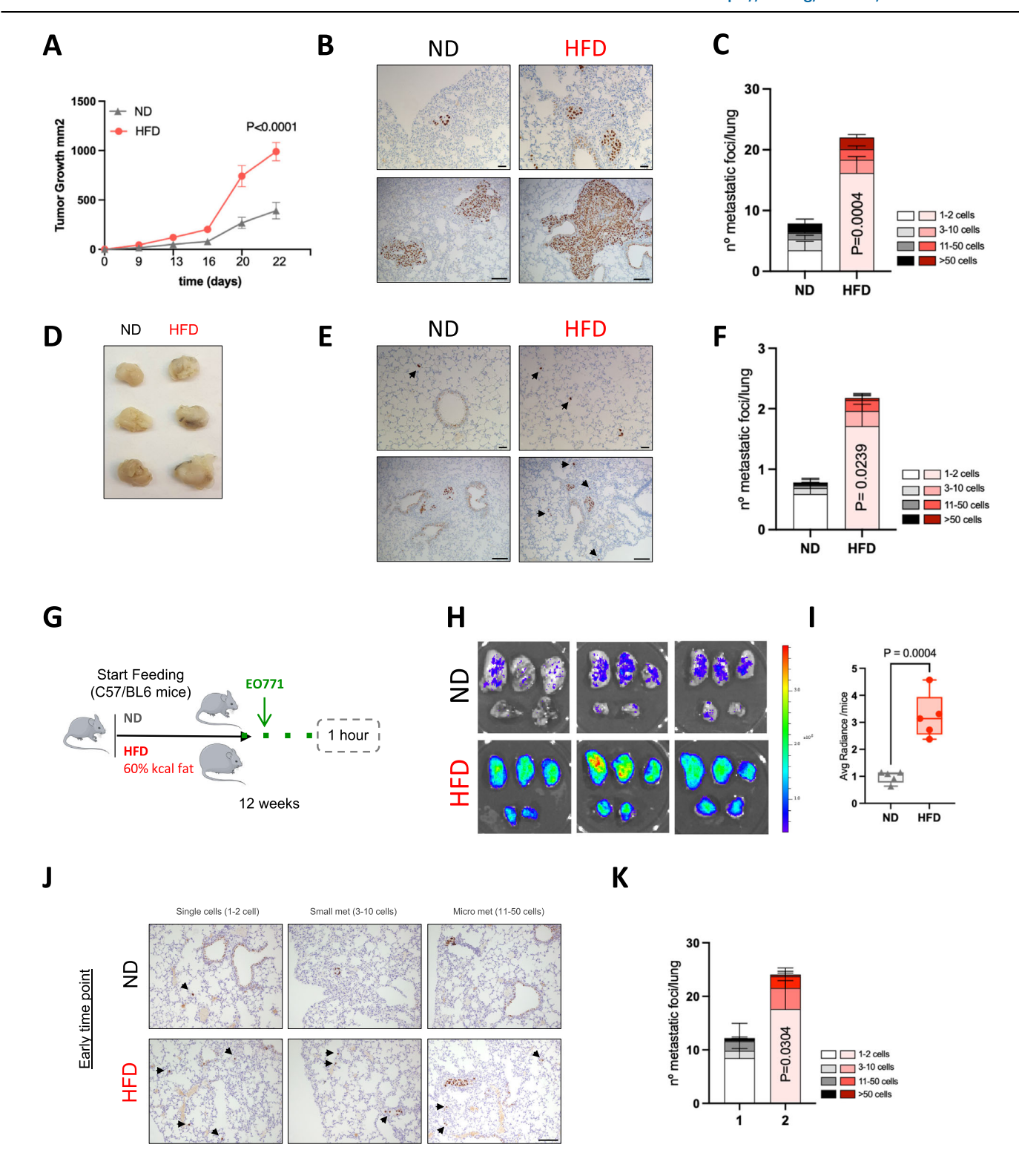
Table 1 | Significant regulated pathways and genes in CD45⁻ CD31⁺ lung endothelial cells from mice under HFD compared to ND – For more detailed information about statistical analysis please see the "methods" section

	Significant upregulated genes with Log2(fold_change)>1 and FDR < 0.05				Significant downregulated genes with Log2(fold_change) <-1 and FDR < 0.05			
	ID	log2(FC)	p_value	q_value	ID ID	log2(FC)	p_value	q_value
Cell adhesion	Pcdhga	4,1017	3,52E-13	3,78E-10	Panx1	-3,7916	2,91E-11	2,25E-08
	Arsb	2,5666	3,92E-06	0,0006	Egfr	-2,4576	1,61E-05	0,0019
	Lims2	1,0409	0,0008	0,0321	Lamb3	-2,3968	9,90E-05	0,0081
	Jam2	0,9780	0,0011	0,0415	Ctgf	-2,2834	1,89E-05	0,0022
	Ctnna1	0,9348	3,53E-07	7,70E-05	Dsp	-2,1828	0,0004	0,0204
	H2-Ab1	0,9209	0,0008	0,0330	Hapln1	-2,1435	0,0005	0,0244
	Ocln	0,6408	6,34E-05	0,0057	Prkci	-1,3802	0,0012	0,0455
					Ntn4	-0,9915	0,0003	0,0170
					Itga6	-0,5405	0,0006	0,0270
Hemostasis	Dpep1	3,5400	7,57E-13	7,55E-10	Maf	-2,8297	3,00E-07	6,65E-05
	Plat	2,2240	1,90E-08	6,82E-06	Pdpn	-2,6405	3,21E-08	1,09E-05
	Scpep1	1,9318	3,99E-07	8,57E-05	Olfm2	-2,4076	9,24E-05	0,0076
	Hgsnat	1,5789	1,64E-05	0,0019	Rem1	-2,1523	0,0004	0,0228
	Fn1	1,5749	0,0004	0,0218	Lamc2	-2,0655	0,0008	0,0328
	Vapb	1,4587	0,0007	0,0299	Nppc	-1,8787	0,0009	0,0375
	Ccm2	1,3538	3,32E-05	0,0035	Ifi27l2a	-1,4245	0,0002	0,0122
	Anks3	1,1549	0,0002	0,0140	Dll4	-1,1535	1,54E-06	0,0003
	Lrpap1	1,0759	6,0187E-06	0,0008				
	Egfl7	1,0288	0,0011	0,0411		,		
	Gja4	0,8674	0,0008	0,0325				
	Ak3	0,8541	0,0003	0,0166				
	Plaur	0,7212	0,0002	0,0148				
Inflammatory response	Klhl6	3,5056	1,26E-13	1,77E-10	Btnl9	-4,6732	2,38E-16	1,10E-12
	Zcchc3	2,0106	0,0009	0,0356	Wfdc2	-2,4425	6,11E-05	0,0055
	Tfe3	1,9208	2,25E-10	1,23E-07	Polr3g	-2,2760	0,0002	0,0143
	Cmip	1,4031	2,44E-05	0,0027	Tnfrsf11a	-2,0271	0,0010	0,0385
	H2-Q5	1,3099	0,0013	0,0460				
	Ikbkb	1,1837	0,0009	0,0361				
	Rfxank	1,1060	0,0004	0,0212				
	Rftn1	1,0675	0,0003	0,0166				
	Tlr3	0,9689	1,33E-05	0,0017				
	Mill2	0,8267	0,0005	0,0235				

RNA analysis

Talin. Talin and Src appeared to be activated in endothelial cells after their interaction with platelets from HFD mice⁴⁴ (Fig. 4L). Whether the effect on endothelial cell adhesion was dependent on HFD-induced FN was assessed in a tumor-endothelial adhesion assay using platelets from HFD-fed mice in the presence or absence of FN-neutralizing

antibodies (Fig. 4M). Adhesion of EO771 cells to HUVECs in the presence of blocking antibodies was reduced by 61% relative to that of HUVECs preconditioned with platelets from HFD mice (Figs. 4M, N), suggesting that FN is involved in the adhesion of tumor cells to endothelial cells promoted by platelets from HFD-fed mice.



It is known that integrin $\alpha 5\beta 1$ is the primary FN receptor responsible for cell migration and adhesion^{45,46}. Integrin $\alpha 5\beta 1$ -FN interactions are of particular interest since they contribute to cancer metastasis, as witnessed by its upregulation in invasive cancer cells^{47–49}. Both subunits of this receptor were expressed in our BC cell models, with particularly high levels in the highly metastatic EO771 cells (Suppl. Figure 5A). To demonstrate the relevance of this integrin interaction, we blocked integrin $\alpha 5$ expression in EO771 cells (Suppl. Figure 5B) and performed tumor homing assays (Fig. 4O). The absence of integrin $\alpha 5$ significantly

dampened metastatic cell homing (Fig. 4P), highlighting the significance of this integrin in tumor cell homing to PMNs in HFD mice.

A dietary switch modulates platelet activation and aggregation, and their interaction with endothelial cells

We next investigated whether the effects of a HFD were reversible by subjecting mice to a "diet resting" protocol (S.Diet) in which mice were fed for 12 weeks with a HFD and then switched them to a ND (Switchdiet) for 7 days (Suppl. Figure 5C). We first verified that mice

Fig. 3 | **HFD** enhances tumor cell homing and metastasis to the lung. A Primary tumor growth of EO771 cells injected into the mammary fat pad of ND or HFD-fed. 3 independent experiments: ND n = 16 mice, HFD n = 17 mice. **B** Representative images of p53 staining in the lungs of ND and HFD mice on day 22 post-tumor cell injection (p.i.) Bar: 200 μm. **C** Quantification of the total number of metastatic foci in the experiment shown in (**A**). Lesions were binned into four size categories based on the number of tumor cells: 1-2 cells, 3-10 cells, 11-49 cells, and ≥50 cells. 3 independent experiments: ND n = 15, HFD n = 17 mice. **D** Representative images of tumors from ND and HFD mice on day 14 p.i. (no significant differences in tumor size). **E** Representative images of p53 stained lungs from ND and HFD mice on day 14 p.i. Bar: 200 μm. **F** Quantification of the total number of metastatic foci in the lungs of ND and HFD mice on day 14 p.i. Lesions were binned and analyzed as in (**C**). 4 independent experiments: ND n = 21. HFD n = 28 mice. **G** Scheme illustrating the

EO771 cell homing assay corresponding to **(H). H** Representative images of the 1-hour homing assay with EO771 -GFP-luciferase tumor cells injected into the tail vein of ND and HFD mice. **I** Quantification of experiment in **(H)**, 3 independent experiments, n=12 mice per group. **J** Representative pictures of p53 staining in the lungs of ND and HFD mice at day 14 p.i. Bar: $100 \, \mu \text{m}$. **K** Quantification of the total number of metastatic foci in the lungs of ND and HFD mice at day 14 p.i. by tail vein injection. Lesions were binned and analyzed as in **(C)**, corresponding to 3 independent experiments: n=15 mice per group. All data represent the mean \pm s.d., and the P values were calculated by two-way ANOVA in **(A)** and with a two-tailed Student's t-test in **C**, **F**, **I**, and Mann-Whitney test in **(K)**. Values are shown in box-and-whisker plots where the line in the box corresponds to the mean. Boxes extend from the minimum to the maximum value.

experienced a significant average weight loss of 10% after switching diet (Suppl. Figure 5D) and subsequently, this switch was seen to dampen the activation of platelets, as witnessed by the weaker expression of activated integrin $\alpha_{IIb}\beta_3$ and P-Selectin in platelets from the S.Diet mice (Fig. 5A, B). Consistent with the earlier observations, platelet aggregation was also significantly reduced after switching diet (Fig. 5C). The expression of FN in the plasma and platelets of all the mice was assessed (Fig. 5D-F) and interestingly, FN expression returned to normal in platelets (Fig. 5F) after the resting period (S.Diet) while that in the plasma remained relatively constant (Fig. 5E). We also analyzed the impact of the S.Diet on the adhesive properties of tumor cells to platelet-activated endothelium in vitro (Fig. 5G). As observed previously, the HFD heightened the platelet-endothelial interaction, while in mice that underwent S.Diet, the platelet endothelial interaction was dampened relative to HFD mice (Fig. 5H). Importantly, the normalization of these interactions by switching diet also significantly reduced the adhesion of EO771 tumor cells to endothelial cells (Fig. 51). Overall, the S.Diet positively influenced mice by reducing platelet activation/aggregation, restoring the FN levels in platelets and normalizing the interaction with endothelial cells, reducing their adhesion to tumor cells.

The dietary switch might modify the signaling pathways downstream of FN in endothelial cells, specifically those involving Src and Talin^{41,50}. Indeed, the S.Diet significantly dampened FN expression in endothelial cells (Fig. 5J, K), in conjunction with a reduction in Src activation (Fig. 5J, L). We also observed weaker talin activation, albeit not significantly (Fig. 5J, M). Based on these findings, diet appears to modulate both the activation and aggregation of platelets, changes concomitant with a normalization of FN expression in platelets, limiting the interaction of these cells with tumor and endothelial cells, and the ensuing downregulation of downstream signaling pathways.

A dietary switch or platelet-blocking antibodies dampen breast cancer cell homing and metastasis

We next investigated whether a dietary switch could affect tumor cell homing 1 hour after injection of tumor cells. We observed tumor cell homing was enhanced in the HFD mice (Fig. 6A, B), although it was significantly reversed after a dietary switch (Fig. 6A, B). We also examined the impact of the S.Diet on lung vascular leakiness and while the HFD significantly increased vascular leakiness (Fig. 6C, D), dextran leakiness tended to revert in the S.Diet mice, albeit not significantly (Fig. 6C, D). Hence, while diet may modulate platelet activation and tumor cell homing, endothelial cell function did not appear to be completely restored by dietary switching. This data suggests that tumor cell homing is mainly affected by platelet activation rather than vascular permeability. In addition, we analyzed the effect of diet switching on experimental metastasis by examining lung metastases. Notably, the dietary change led to a significant reduction in tumor cell metastasis within one week (Fig. 6E, F), indicating that diet switch dampens platelet activation and thereby affects both tumor cell homing and metastasis.

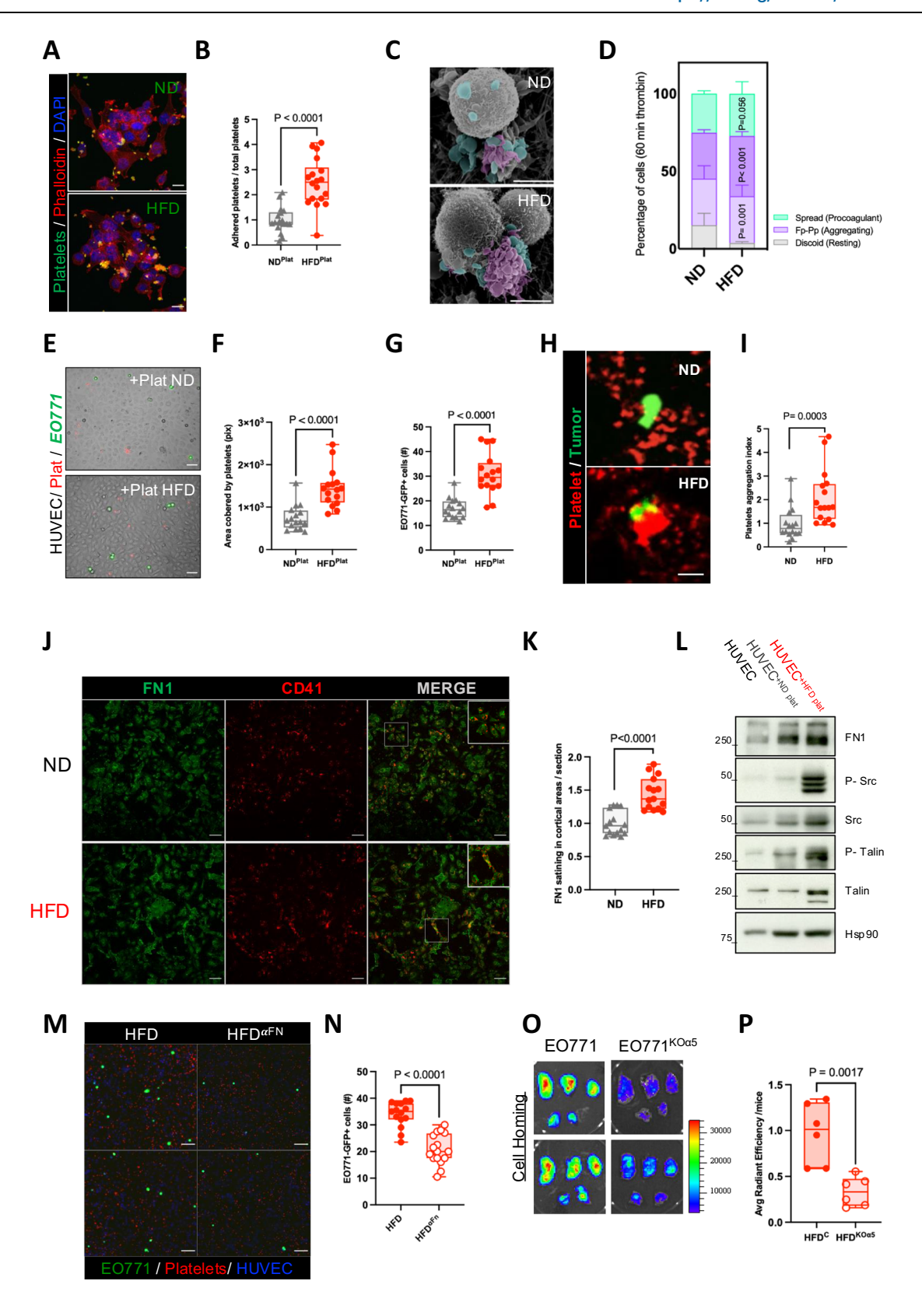
To analyze the relevance of platelets in tumor cell homing after HFD-induced PMN formation, we depleted platelets in HFD mice prior to the injection of tumor cells using anti-GPIbα (R300) antibodies⁵¹ (Suppl. Figure 5E). Mice received a single R300 injection 48 hours before that of the tumor cells, inducing a window of platelet depletion just when tumor cells home to the PMNs. After verifying platelet depletion, tumor cells were injected into the tail vein and tumor cell homing was analyzed 1 hour later (Supp. Figure 5E). Platelet depletion promoted a significant decrease in tumor cell homing in HFD and in ND mice (Fig. 6G, H), although the reduction was not significant in the latter. The effect of platelet depletion 48 hours before tumor cell injection on experimental metastasis assays in HFD mice was also analyzed in the lungs after 21 days (Fig. 6I-J). Importantly, the R300 antibody not only dampened tumor cell homing but also metastasis in HFD mice, yet not in the ND mice (Fig. 6J). Hence, platelets appear to be crucial to promote tumor cell interactions at PMNs. The activation of platelets in these niches by a HFD can be reversed by a dietary switch or platelet depletion during PMN formation, offering potential therapeutic strategies to reduce tumor cell homing to PMNs.

Disease outcome is worse in TNBC patients with hypercoagulation prior to surgery

Since a HFD appears to promote platelet activation and aggregation, a HFD and increased BMI might also affect the coagulation profile in this model. Thus, the blood coagulation profile was analyzed in ND and HFD mice, measuring the Prothrombin Time (PT: Fig. 7A), Partial Thromboplastin time (aPTT:Fig. 7B), Thrombin Time (TT: Fig. 7C) and Fibrinogen (Fg:Fig. 7D) in the DIO model. Of all the parameters analyzed, the aPTT was significantly reduced in HFD mice (Fig. 7B).

Based on our hypothesis and the association between a high BMI, pro-thrombotic risk and cancer⁴, we analyzed the potential association of BMI and coagulation parameters with disease outcomes in patients with TNBC. TNBC has an elevated risk of metastatic disease development and lower survival rates than hormone-positive BC52. Moreover, being overweight is associated with a shorter disease-free and overall survival time among TNBC patients⁷. Hence, the correlation of BMI and different coagulation parameters before surgery with disease outcome was analyzed in a cohort of 82 early TNBC patients treated, with neoadjuvant and/or adjuvant chemotherapy. The PT, aPTT, INR (International Normalized Ratio), Fg and platelet counts were evaluated in TNBC patients prior to surgery, examining the correlation between these parameters and the BMI. The BMI was inversely correlated with a reduced aPTT, albeit moderately (Fig. 7E), whereas no significant correlation was observed between the BMI and platelet count, platelet volume, total Fg or the INR.

Further analysis of these parameters relative to disease outcome demonstrated that patients with the shortest aPTT (1st Quartile - Q1) experienced a significantly shorter time to relapse (estimated mean time to relapse of 8.5 years) than other patients (11.9 years, P = 0.0014: Fig. 7F). However, a multivariate analysis did not reveal any further correlations of BMI with disease outcome or among the other



parameters that were related to higher coagulation profile (Fig. 7G–I): PT, p = 0.568; INR, p = 0.789; or Fg, p = 0.135. Overall, these data suggest that although BMI was inversely correlated with a shorter aPTT, only a shorter aPTT could be considered as an independent additional risk factor of disease progression in TNBC patients prior to neoadjuvant treatment and surgery.

Discussion

There is considerable experimental evidence that platelets influence metastasis^{17–19,21,53} and early metastatic dissemination^{20,21}, therefore this study set out to assess the influence of additional systemic cancer risk factors in platelet-driven BC metastasis, in particular that of a HFD. The data obtained suggest that a HFD increases the activation, adhesion

Fig. 4 | **A HFD reinforces tumor-platelet-endothelial cell interactions. A** Representative images showing EO771 tumor and platelets. Bar: 15 μ m. **B** Quantification of (**A**), 2 independent experiments: ND n = 18, HFD n = 17 fields per group. **C** Representative SEM images showing EO771 tumor cells and platelets. Bar, 20 μ m. **D** Quantification of **C**. (>150 platelets per experiment), showing the mean \pm SEM of each morphology. 2 independent experiments: n = 12 images per group. **E** Representative images of EO771 tumor cell adhesion to endothelial cell monolayers stimulated by platelets. Bar: 50 μ m. **F** Quantification of the endothelial cell surface area covered by platelets. 2 independent experiments, n = 16 fields per group. **G** Quantification of the number of EO771-GFP cells (#) adhered to endothelial cells incubated with platelets, 3 independent experiments: n = 16 fields per group. **H** Representative images by intravital microscopy of EO771-GFP cells and platelets. Bar, 30 μ m (**I**) Quantification of **H**, n = 4 mice per group, 16 independent positions. **J** Representative images of immunofluorescence staining for FN1 and

CD41 in HUVEC cells incubated with platelets for 16 h. Bar, 100 μ m. **K** Quantification of cortical FNI staining from the experiment in (**J**) 2 independent experiments: n=15 fields per group. **L** Representative Western blot images in HUVEC cells after a 16 h incubation with platelets. N = 3 independent experiments. **M** Representative images of EO771-GFP cells, platelets and HUVEC cells incubated for 16 h with platelets from HFD mice in the presence or absence of the anti-FN1 antibody. Bar, 100μ m. **N** Quantification of (**M**). 2 independent experiments: ND n=15, HFD n=16 fields. **O** Representative images of the homing assay with EO771 and EO771-KO α 5 tumor cells injected tail vein of HFD mice. **P** Quantification of (**O**), 2 independent experiments: n=11 mice per group. Data represent the mean \pm s.d., and P values were calculated by Mann-Whitney test in (**F**, **I**, **K**) and with a two-tailed Student's t-test in (**B**, **D**, **G**, **N** and **P**). Values are shown in box-and-whisker plots where the line in the box corresponds to the mean. Boxes extend from the minimum to the maximum value.

and the aggregation of platelets in circulation, and in the lungs of mice, leading to hypercoagulation.

Obesity is known to promote prothrombotic signaling in relation to platelet activation and hypercoagulability54,55. Our findings reveal that Src and Talin are activated in platelets obtained from HFD mice, and in endothelial cells exposed to platelets from these mice. Interestingly, the activation of Src is involved in the activation of platelets⁵⁶ and endothelial cells⁵⁷, promoting the recruitment of several proteins like Talin and integrins58, the latter serving as receptors for ECM molecules like FN⁵⁹. Moreover, it is worth noting that prolonged Src activation has been implicated in disrupting barrier permeability⁵⁷. Hence, these findings support a model in which a HFD induces Src hyperactivation and Talin expression in both platelets and endothelial cells, leading to increased vascular permeability and platelet activation, and enhancing tumor cell interactions through the upregulation of FN. Furthermore, our data also suggests that platelets from HFD mice exhibited prolonged phosphorylation, both inside-out and outside-in, producing elevated levels of pSrc and pPKC. By contrast, Src is partially inactivated in the inside-out pathway in platelets from ND mice, and activated again in the outside-in pathway, whereas Src exhibited constant activation in platelets from HFD mice. Src phosphorylation can induce filopodia and lamellipodia formation during platelet spreading by mediating calcium signaling and PKC activity⁶⁰, while PKC and AKT are important regulators of platelet granule secretion^{28-30,61}. The data obtained here suggests the pre-activation of inside-out signaling pathways in HFD mice, and more rapid outside-in signaling upon stimulation. It is worth noting that this type of activation has been associated with adhesion to the vascular wall and platelet aggregation⁶².

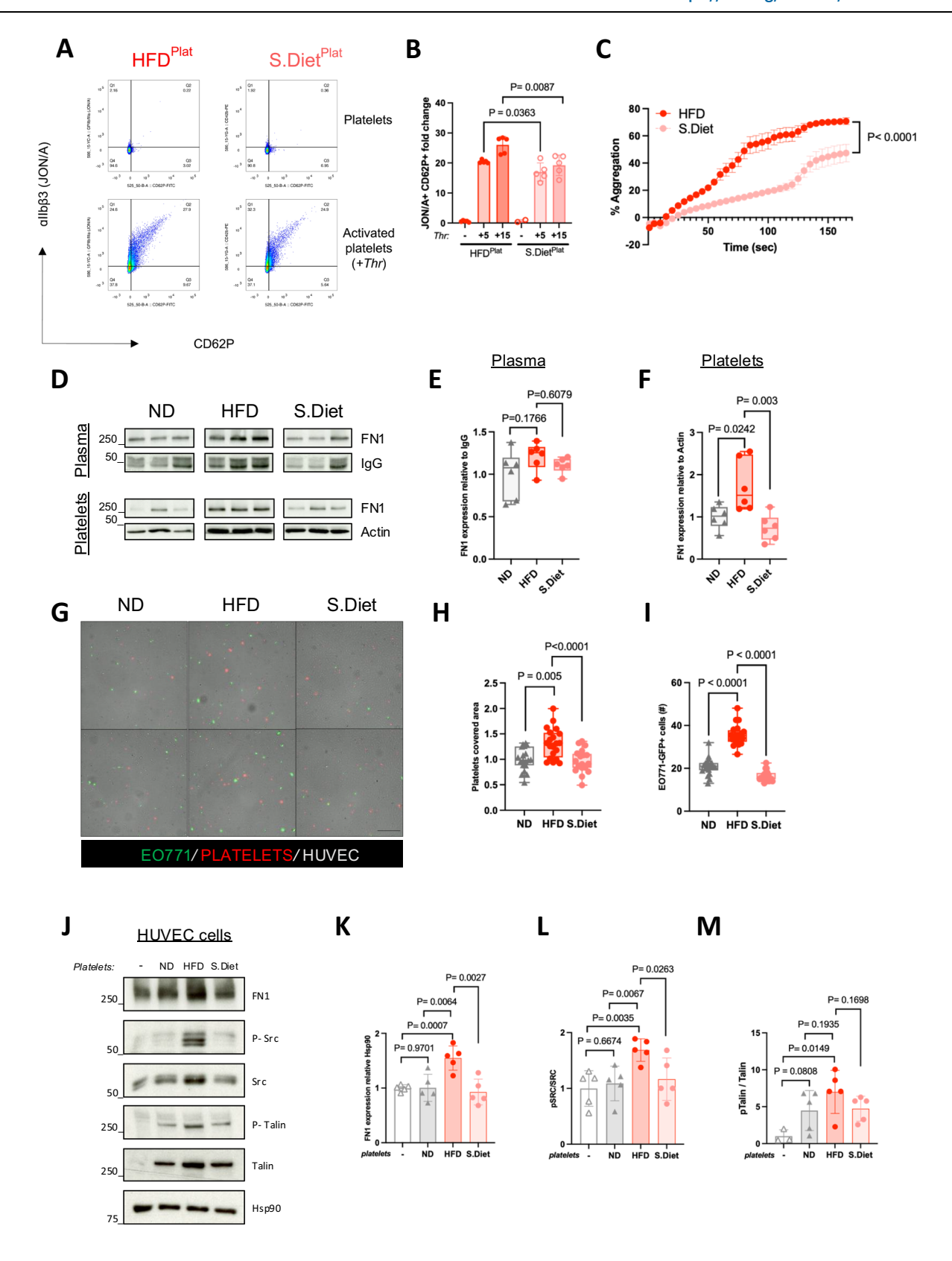
In addition to platelet activation and aggregation, the HFD increased vascular leakiness, modulating the expression of genes associated with cell adhesion and platelet activation, and endothelial cell damage 63,64. These results are consistent with studies indicating that vascular injury leads to a shift in the endothelium from an anticoagulant to a procoagulant phenotype, resulting in the exposure of fibers and other endothelial matrix proteins 65,66. Indeed, studies have shown that obesity enhances vascular leakiness, thereby promoting BC extravasation 67. Our data suggests that systemic changes induced by HFD could affect the generation of PMNs, changes that influence vascular leakiness, platelet activation and ECM remodeling, favoring tumor cell homing and metastasis. Interestingly, similar changes have been proposed as hallmarks of PMN formation by primary tumors 22, suggesting that they may be shared between these microenvironments.

We identified FN as a key molecule upregulated in endothelial cells and activated platelets in the lungs, both in vitro and in vivo. There are two forms of FN, plasma FN (pFN) that lacks extra EDA and EDB segments, and tissue cellular FN (cFN) that is synthesized by many cell types (e.g., fibroblasts, endothelial cells, platelets and monocytes)

and that bears varying proportions of EDA and EDB segments⁶⁸. Both forms of FN can be incorporated into the fibrillar network of the ECM⁶⁸. Of these, pFN supports hemostasis and regulates thrombosis⁶⁹, while cFN is implicated in efficient adhesion, activation and aggregation of platelets, promoting inflammation and thrombosis^{70–72}. We found that the overexpression of FN in platelets induced by a HFD is crucial in regulating the interaction between platelets, endothelial and BC cells.

Moreover, FN plays a critical role in PMN formation³⁷ and lung metastasis73. Interestingly, cFN levels are significantly elevated in the plasma of patients with thromboembolism or diabetes⁷⁴ and they are positively correlated with the BMI⁷⁵. The results here support the notion that platelets play a crucial role for successful vascular retention and metastatic outgrowth, consistent with an effect of HFD on platelets that enriches FN, influencing tumor cell homing and metastasis. These observations are supported by previous studies on FN-EDA KO mice administered a HFD, which exhibit reduced thromboembolism relative to WT mice on the same diet. Hence, FN appears to promote thromboembolism in the context of DIO⁷⁵. Interestingly, an ECM rich in FN primes endothelial cells for activation in response to oxidized low-density lipoprotein⁷⁶ and hyperglycemia⁷⁷. Furthermore, atheroprone shear stress has been implicated in the upregulation of FN expression creating a positive feedback loop that sustains endothelial cell inflammation⁷⁸. A HFD appears to promote platelet activation and aggregation at PMNs, concomitant with FN overexpression and deposition at their surface, that interacts with integrin $\alpha 5\beta 1$ receptors on tumor cells. The involvement of integrin $\alpha 5\beta 1$ in tumor cell migration, invasion and metastatic tumor cell homing makes it an attractive therapeutic target^{47–49,79}. However, given the complexity of obesity-associated inflammation and BC metastasis^{8-10,80}, and the multifaceted role of platelets in PMNs81, the mechanisms driving FN overexpression at PMNs are likely to be multifactorial⁵⁴. Consistent with previous studies³⁹, we observed that adipose tissue from HFD-fed mice secretes elevated levels of TNF-α. Notably, this factor promoted FN expression and accumulation in platelets, suggesting an additional mechanism underlying FN expression in circulating platelets from HFD-fed mice. Furthermore, given the crucial role of FN in platelet aggregation and activation^{70,82}, our findings support a model in which HFD-induced signaling enhances platelet FN uptake and retention, potentially contributing to the prothrombotic state associated with HFD-fed mice.

It is widely accepted that obesity is associated with a higher incidence of BC, and with increased mortality and metastasis^{6,7}. While several studies have shown that obesity is associated with BC metastasis^{8,9,80}, the impact of platelets in this process has not been thoroughly assessed. Our data demonstrates a distinct role for platelets in the obese microenvironment, primarily influencing tumor cell homing and subsequently impacting later stages of metastasis. We found that the tumor cells in HFD mice have a greater capacity to extravasate and successfully survive as solitary cells in the lung



parenchyma when compared to those in ND mice. We also found that platelets from HFD mice adhere more efficiently to both tumor cells and endothelial cells, rapidly binding to these upon their homing to metastatic organs and resulting in the formation of significantly larger aggregates. One possible explanation could be that after they home to the target organ, tumor cells are protected from the action of immune cells (e.g., NK cells) by the surrounding platelets, as

suggested elsewhere¹⁸. Nevertheless, we did not analyze the implication of immune cells in this system, and the mechanism by which a HFD may lead to platelets favoring individual cell metastasis remains unclear.

Importantly, our findings indicate that the platelets derived from HFD mice interact more strongly with cells from both high and low metastatic TNBC models, although a HFD specifically reinforces single

Fig. 5 | **A dietary switch restores fibronectin levels and reverts tumor cell homing to the lungs. A** Flow cytometry analysis of platelet activation, measuring the expression of activated α IIbβ3 (JON/A) and P-Selectin (CD62P) in the absence (Resting platelets) and presence (Activated platelets) of thrombin (0.05 IU/m) from the mice following a HFD or S.Diet. **B** Graph of the quantification of the experimental data shown in A. 5 independent experiments: n = 3 platelet samples per group. **C** Aggregation of platelets obtained from both HFD and S.Diet mice, and their response to thrombin (0.01 IU/m). The data correspond to 3 independent experiments: ND n = 10, and HFD n = 8 platelet samples. **D** Representative Western blots analyzing FNI expression in plasma (top panels) and platelets (bottom panels) from ND, HFD and S.Diet mice. **E**, **F** Quantification of FN1 expression in the plasma (**E**) and platelets (**F**) from the data shown in D, corresponding to 2 independent experiments: n = 6 platelet samples per group. **G** Representative images of EO771 cell adhesion (green) to endothelial cell monolayers stimulated with platelets (red)

from ND, HFD and S.Diet mice. Bar: $100 \, \mu m$. H Quantification of the endothelial cell surface area covered by platelets obtained from ND, HFD and S.Diet mice (shown in G). I Quantification of the number of EO771-GFP cells (#) adhered to endothelial cells stimulated with platelets from ND, HFD and S.Diet mice (shown in G). 2 independent experiments: n = 20 fields analyzed per group. J Representative Western blots detecting FN1, p-Src, Src, p-Talin, Talin, and Hsp90 expression in HUVEC cells after a 16 h incubation with platelets from ND, HFD and S.Diet mice. K-M Graphs of the quantification of the experimental data shown in (J), n = 5 independent experiments. All the data represent mean \pm s.d., and P values were calculated by two-tailed Student's t-test in (B, K, L, M) one-way ANOVA in (E, F, H, I,) and two-way ANOVA in (C). Values are shown in box-and-whisker plots where the line in the box corresponds to the mean. Boxes extend from the minimum to the maximum value.

cell homing only in highly metastatic models. Hence, both extrinsic and intrinsic characteristics of the cancer cells appear to play an important role in this process. Notably, platelets engage with cancer cells and form stable aggregates primarily through the expression of P-selectin^{83,84}. Indeed, platelets derived from HFD mice not only exhibit enhanced P-selectin expression but also, their interactions with tumor cells are heightened both in vitro and in vivo. In addition, we observed that platelets from HFD-fed mice, aside from being more activated, also exhibited an enhanced spreading phenotype when interacting with tumor cells compared to platelets from ND-fed mice. These findings align with previous studies showing that platelet shape is modified upon contact with tumor cells⁸⁵ and further demonstrate that platelets from HFD-fed mice display a heightened activation status while on the surface of tumor cells.

Once cancer cells have disseminated, their ability to home to a supportive niche becomes crucial for successful metastasis 22 . While a HFD appears to influence tumor cell interactions with endothelial cells in mice, the data presented here suggest that dietary intervention can reverse or mitigate certain consequences of a HFD. However, vascular damage appears to be more persistent and may require additional time to recover completely, as indicated elsewhere 10 . These findings imply that the impact on cell dissemination in HFD mice is probably due to the diet itself rather than solely being a result of high adiposity. Strikingly, the data from the ob/ob mouse model supports the notion that high adiposity induces increased vascular leakiness, regardless of diet.

While several studies suggest that weight loss is associated with improved BC outcomes⁸⁶, the impact of diet on coagulation and metastasis has been little studied. Remarkably, the dietary switch restored FN levels concomitant with a decrease in lung metastasis. However, it is noteworthy that vascular injury persisted even after weight loss over the period analyzed here, probably due to the systemic effects of inflamed adipose tissue. These data highlight the complex interaction between diet and metastasis, such that vascular leakiness alone is not sufficient to affect tumor cell homing and that further factors are also required, for example platelet activation. It would be interesting to analyze coagulation parameters and clinical outcomes in ongoing clinical studies on dietary intervention in BC as an additional clinical factor.

From a clinical perspective, our study demonstrates that TNBC patients with stronger hypercoagulation have a worse prognosis. Although no direct association with BMI was seen, HFD mice and patients with a higher BMI had shorter aPTTs. Given the role of platelets in hematogenous metastasis, interest has grown in developing drugs that target platelets for anti-tumor therapy. Most of these drugs focus on inhibiting platelet activity and thus, they have the drawback that other platelet functions may be affected⁸⁷. Our study demonstrates that a dietary switch or depleting platelets reduces metastasis in the lungs of mice on a HFD. Platelet depletion was particularly successful in reducing metastasis that developed on a background of a HFD right before tumor cell homing. Interestingly, aspirin treatment

during tumor cell homing, yet not after tumor cell extravasation, reduces lung metastasis by inhibiting the platelet-derived COX-1/thromboxane A2 axis s. It would be interesting to test other antiplatelet drugs, such as inhibitors of $\alpha_{Ilb}\beta_3$ and selectins in this context since their effect on cancer progression has yet to be evaluated since their effect on cancer progression has yet to be evaluated fundings support the effectiveness of anti-platelet therapies in blocking tumor cell homing, particularly in HFD-induced microenvironments. It should be recognized that other anti-coagulant treatments may affect later stages of metastasis, as previously suggested elsewhere since later stages of metastasis, as previously suggested elsewhere since later stages of metastasis, as previously suggested elsewhere since later stages of metastasis. However, evidence of the effective clinical use of anticoagulant and anti-platelet drugs in obese patients and in the premetastatic setting is limited.

Method

Patient samples

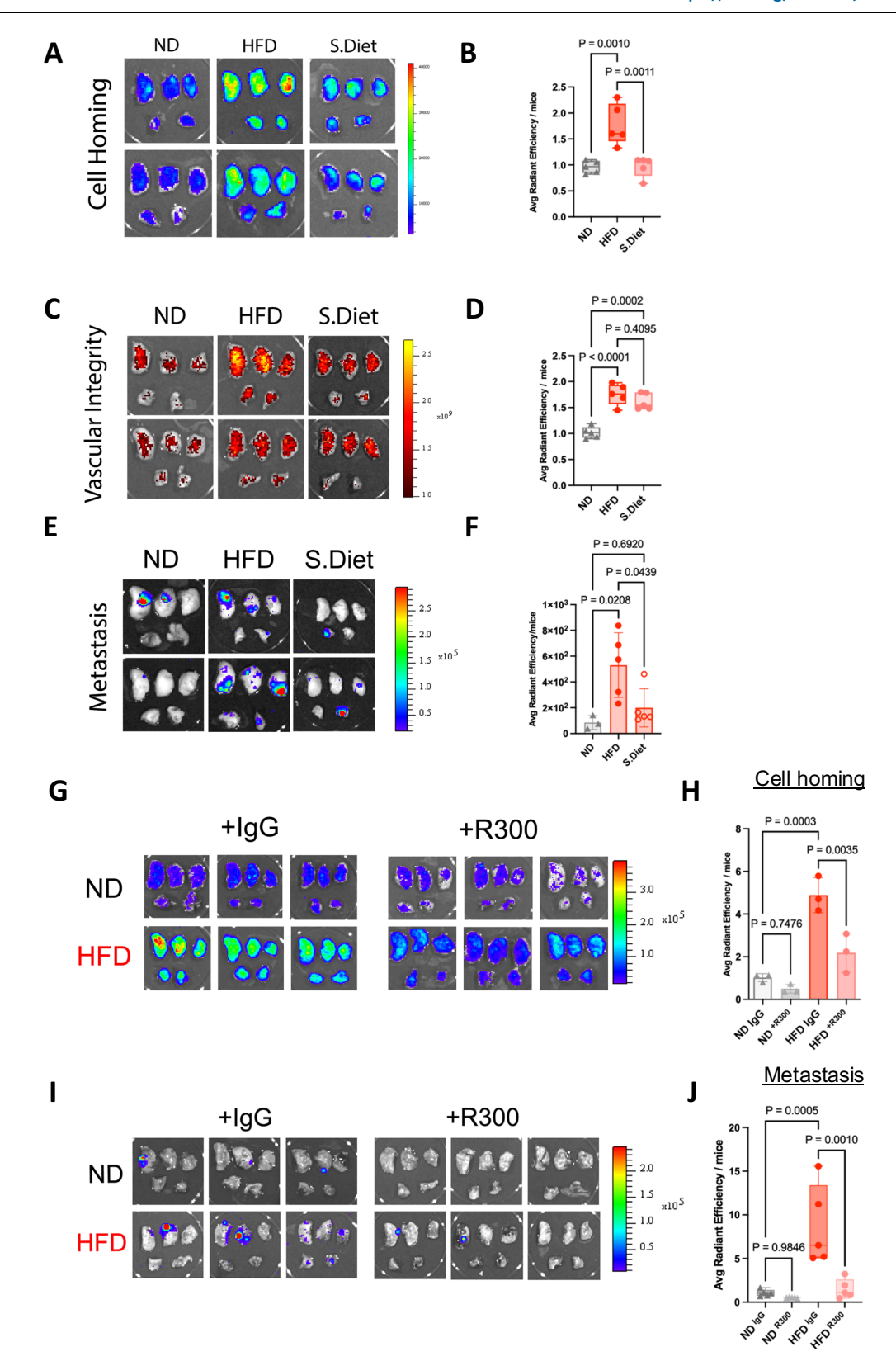
The human studies performed here were all approved previously by the ethics committees from the Hospital Universitario de Fuenlabrada (protocol approval number CEI: 11/37). The study included one cohort of 82 patients diagnosed with early TNBC between 2012 and 2015, and who were eligible for neoadjuvant and/or adjuvant chemotherapy. The diagnosis was based on negative expression of ER/PR (less than 10%) by immunohistochemistry (IHC) and HER2, either IHC 0-1 or fluorescent in situ hybridization (FISH)-negative if ≥ 2 on IHC (see Suppl. Table 2 for the clinical characteristics of the patients). The PA clinical study protocol was approved to gather their clinical, demographic and blood test data, and all the participating patients signed an informed consent form. The study was carried out in accordance with the Helsinki Declaration and approved by the Institutional Review Board. TNBC was defined as negative (<1%) for ER and PR expression, and no amplification of HER2 (result of 0+ or 1+ in an Herceptest or a result of 2+ with negative FISH).

Inclusion and ethics statement

There were no restrictions regarding gender or ethnicity in our protocol; however, the recruited population was primarily Caucasian and Hispanic due to the local demographics.

Animal studies

All the experimentation with mice was first approved by the Institutional Ethics Committees of the CNIO (IACUC-015-2017, IACUC-020-2018, IACUC-017-2022), the Instituto de Salud Carlos III (CBA-19_2017, CBA 01_2019v4, CBA-04_2023v2) and the Comunidad Autónoma de Madrid (PROEX 227/17, PROEX091/19, PROEX77.1/23). The maximum tumor size (1000 mm³) and burden permitted by our ethics committee were not exceeded in the subcutaneous and metastasis models. All the experiments on animals were performed in accordance with the guidelines for ethical conduct in the care and use of animals, as stated in the International Guiding Principles for Biomedical Research



involving Animals and devised by the Council for International Organizations of Medical Sciences.

Diet-induced obesity (DIO) model

C57BL/6JolaHsd male and female mice and C57BL/6-Tg (CAG-EGFP) 10 sb/J male (8–12 weeks old: Envigo and Jackson Laboratory) were used in these studies, and they were housed at 21 ± 2 °C with 50-60%

humidity, on a13 h light and 11 h dark cycle. For studies on male mice, 8-week-old mice were maintained on either a high-fat (HFD, 60% kcal, Research Diet D12492) or standard (ND, 6.2% Kcal, Envigo 2018S) diet for 12 weeks. For studies on female mice, 8-week-old mice were maintained on either a high-fat (HFD, 60% kcal, Research Diet D12492) or low-fat (LFD, 4% kcal, Envigo 2014) for 20 weeks. The key experiments (i.e., vascular leakiness, tumor cell homing, experimental

Fig. 6 | **Platelet depletion reduces breast cancer cell homing and metastasis in mice following a HFD. A** Representative bioluminescence images 1 hour after EO771-Luc tumor cell tail vein injection in ND, HFD and S.Diet mice. **B** Quantification of the average radiance per mice in the experiment shown in (**A**). 3 independent experiments: ND n = 11, HFD n = 12, and S.Diet n = 13 mice. **C** Representative images of vascular permeability in the lungs of ND, HFD and S.Diet mice using NIR-Dextran. **D** Quantification of NIR-Dextran fluorescence from the experiments in (**C**). 2 independent experiments: ND n = 8, HFD n = 8, and S.Diet n = 9 mice. **E** Representative bioluminescence images from the metastasis assay with EO771 tumor cells injected into the tail vein of HFD and S.Diet mice. **F** Quantification of the average radiance per mice from the experiment shown in (**E**), corresponding to 2 independent experiments: ND n = 6, HFD n = 9, and S.Diet

n = 10 mice. **G** Representative bioluminescence images of EO771-Luc cells injected into the tail vein 48 hours after R300 antibody treatment of ND and HFD mice during metastatic homing assays. **H** Quantification of the average radiance per mice from the experiment shown in (**G**). 2 independent experiments: n = 5 mice per group. **I** Representative bioluminescence images of EO771-Luc cells injected into the tail vein 48 hours after R300 antibody treatment of ND and HFD mice in metastasis assays. The metastases were analyzed 21 days p.i. **J** Quantification of the average radiance per mice from the experiment shown in (**I**). 2 independent experiments: ND n = 9, ND + R300 n = 9, HFD n = 8, ND + R300 n = 8. All the data represent the mean \pm s.d. and the P values were calculated by One way ANOVA. Values are shown in box-and-whisker plots where the line in the box corresponds to the mean. Boxes extend from the minimum to the maximum value.

metastasis, platelet parameter analysis, platelet aggregation analysis) were performed on both sexes of the DIO model and we did not find differences between sexes. Weight was monitored throughout the experiments. At the end-point, animals were either euthanized for coagulation analysis or injected with NIR-dextran (see Permeability assay with NIR-Dextran) or tumor cells (see sections on primary tumor growth and spontaneous metastasis, and experimental metastasis assay). For the dietary switch (HFD/ND-LFD), 8-week-old male or female BL6 mice were fed with a HFD diet until the end of DIO protocol and then switched to the ND or LFD for 1 week prior to sacrifice.

Ob/ob model. To analyze the effects of adipose tissue, 4-week-old female B6.Cg-Lepob (*ob/ob*: Jackson Laboratory) mice were maintained on a normal rodent diet (ND: Envigo 2018S). Their weight was monitored over time from 5 weeks of age and the mice were sacrificed when their weight exceeded 40 g, a period that was significantly shorter (6 weeks) than that of the DIO model (12 weeks). After 6 weeks, the mice were injected with NIR-dextran or tumor cells to perform 1 h homing assays.

In vivo vascular permeability

To prepare NIR fluorescent dextran, 6.5 mg of dextran was diluted in 1.8 ml of 0.1 M NaHCO $_3$, and 190 μ l of DMSO and 10 μ l of cyanine 7.5 NHS ester (25.6 mM) was then added to the solution. The mixture was kept in the dark and stirred at room temperature (RT) for 4 hours, after which the reaction was purified with 50 kDa Amicon filters (filtration 14,000 rpm, 10 min; recovery 7500 rpm, 5 min). The tail vein of male and female DIO mice was injected with 1 mg g $^{-1}$ dextran and lung permeability was analyzed 1 h after dextran injection by bioluminescent imaging (Xenogen IVIS-200 Optical In Vivo Imaging System).

Cell lines and reagents

EO771 cells were purchased from CH3, the Py230 cell line was purchased from the ATCC and HUVECs were obtained from Lonza. Py8119 cells were kindly provided by Dr Cyrus Ghajar (Fred Hutchinson Cancer Center), MC38 cells by Dr Luuke Hawinkels (Leiden University Medical Center) and AT3 cells by Dr Inge Verbrugge (The Netherlands Cancer Institute). The EO771 and AT3 tumor cell lines were grown in high-glucose DMEM (Lonza) supplemented with 10% fetal bovine serum (FBS: Hyclone), 2 mM glutamine and 20 μg ml $^{-1}$ gentamicin. MC38, Py230 and Py8119 cells were grown in Ham's F12 (Lonza) supplemented with 10% FBS (Hyclone), 2 mM glutamine and 20 μg ml $^{-1}$ gentamicin. The HUVEC line (Clonetics, Lonza, Verviers, Belgium) was cultured in EGM-2 medium containing growth factors (Clonetics), 20 μg ml $^{-1}$ gentamicin and 10% (v/v) FBS. Culture flasks were precoated with gelatin 0.2% in ultra-purified water for 15 min and all cells were grown at 37 °C in a humidified 5% CO2/95% air atmosphere.

For *Itga5* gene inactivation, sgRNAs were designed using the Benchling CRISPR sgRNA tool (http://www.benchling.com). Specific sgRNAs were tested against the *Itga5* gene (NM_010577, exons 3 and 4), and also a non-targeting (NT) guide was used as a control. These

sequences were cloned into the lentiCRISPRv2 vector (plasmid #52961, Addgene) and verified by Sanger sequencing. Recombinant lentiviruses were produced by transient plasmid transfection into HEK293T cells using the calcium phosphate method. Cells were transfected using second-generation packaging plasmids (psPAX2 and pMD.2 G, #12260 and #12259, respectively, Addgene) and the appropriate transfer plasmid (pLV CRISPR sg/tga5 or pLV CRISPR sgNT). The medium was collected after 48 hours, cleared by low-speed centrifugation, and filtered through 0.45 µm pore-size PVDF filters (Millipore). Viral titers were calculated by qPCR and values ranged from 10⁷ to 10⁸ TU/ml.

Primary tumor growth and spontaneous metastasis

To investigate the effects of a HFD on breast cancer (BC) primary tumor growth, 1×10^6 BC cells (EO771) were injected into the right thoracic mammary fat pad of 20-week-old female DIO mice. Cells were injected in 1:1 serum-free DMEM/growth factor-reduced Matrigel (BD Biosciences). The tumor volume was measured with a digital caliper and calculated as V = (L \times W²)/2. Key time points throughout the trial were: 0 d, prior to tumor cell injection; 14 d, when primary tumors presented no statistical differences between the groups; 22 d, when primary tumors presented statistical differences between the groups. To assess spontaneous metastasis to the lungs, mice were euthanized on day 14 or 22, and the lungs were fixed with 10% formalin, paraffinembedded, and hematoxylin and eosin (H&E) stained. For EO771 cells, tissue sections (10 μ m) were stained with p53 and metastases were counted using a Leica Aperio digital pathology slide scanner and software.

Experimental metastasis assay

To investigate the effects of a HFD on experimental metastasis to the lungs, 1×10^5 EO771 BC cells labeled with GFP and luciferase (GFP-Luc) were injected into the tail vein of 22-week-old male and female DIO mice. Cells were resuspended in calcium- and magnesium-free PBS, and filtered through a 40 μm mesh immediately prior to injection. Animals were injected with luciferin (3 mg: MB102, syd labs), and lung metastases were then analyzed by bioluminescent imaging (Xenogen IVIS-200 Optical In Vivo Imaging System) 1 h, 24 h, 2 or 5 weeks after tumor cell injection using Living Image 4.7.2 software (PerkinElmer).

Platelet depletion assays

The effect of platelet depletion was analyzed in male DIO mice. Platelet depletion was achieved by injecting a single intravenous dose of an anti-Gp1b α antibody (R300, 4 μ g g⁻¹: Emfret Analytics) or rat IgG2a isotype control (C301, Emfret Analytics) 48 h before tumor cells (1 × 10⁵ EO771 GFP-Luc cells) were injected intravenously. Tumor cell homing was analyzed 1 h after injection by bioluminescent imaging (BLI: Xenogen IVIS-200 Optical In Vivo Imaging System). To analyze the effect of platelet depletion on experimental metastasis, platelet depletion was performed as indicated above 48 h before injecting the EO771 tumor cells (1 × 10⁵ cells). Lung metastases were analyzed over

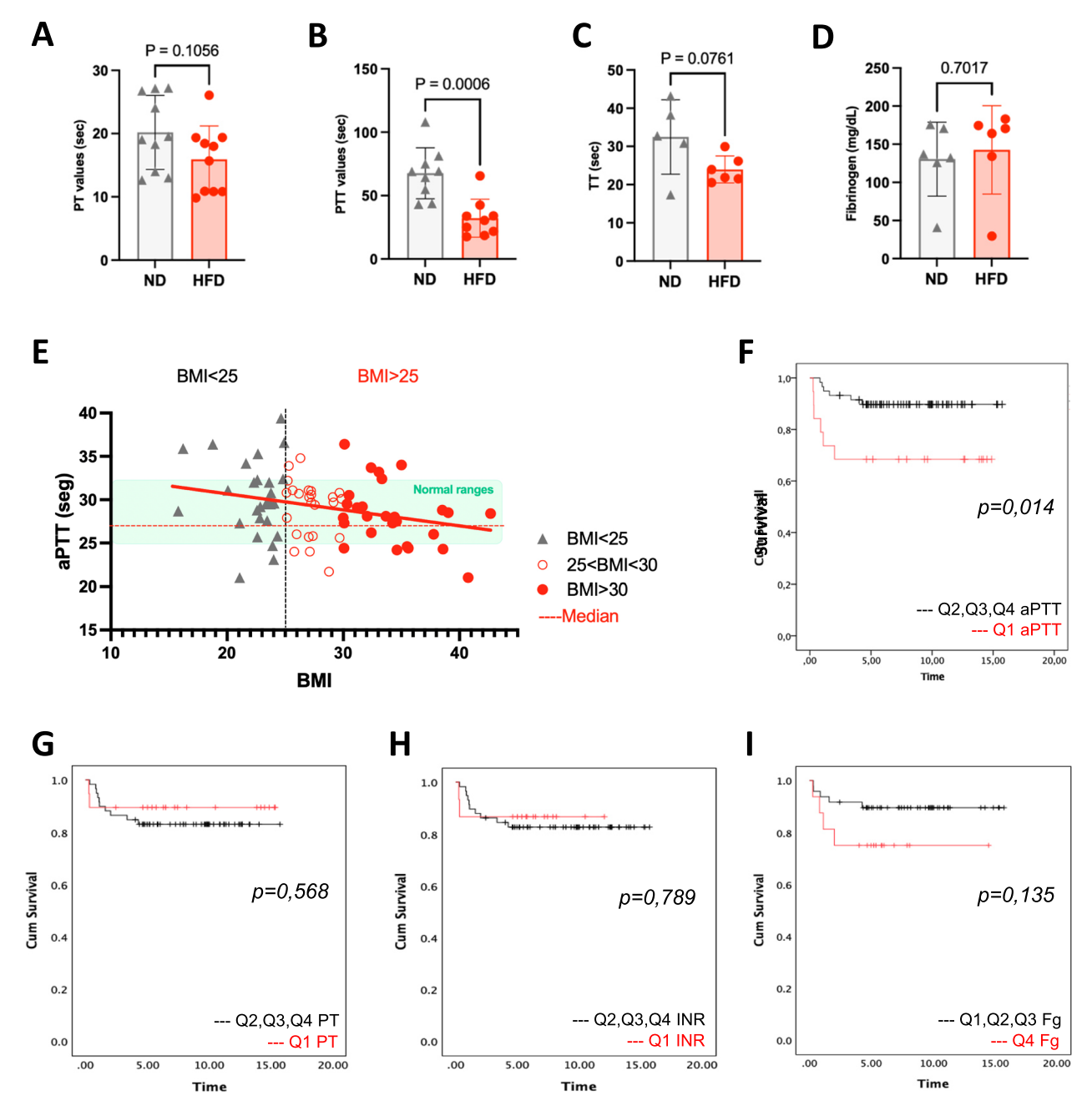


Fig. 7 | **High BMI** is correlated with hypercoagulation and disease progression in TNBC patients. A PT values measured in ND, and HFD mice. 10 independent experiments: ND n = 36, HFD n = 37 mice. **B** aPTT values measured in ND, and HFD mice. 9 independent experiments: ND n = 29, HFD n = 29 mice. **C** TT values measured in ND, and HFD mice. 5 independent experiments: ND n = 14, HFD n = 20 mice. **D** Fibrinogen values measured in ND, and HFD mice. 6 independent experiments: ND n = 28, HFD n = 29 mice. All data is expressed as the mean \pm s.d and P values were calculated with two-tailed Student's t-test in (**A**, **B**, **C** and Mann-Whitney test in **D**). **E** Plot of BMI vs aPTT values among TNBC patients. Patients with

BMI < 25 were categorized as normal weight and patients with BMI > 25 were categorized as overweight or obese. BMI > 25 is a positively correlated with a lower aPTT (correlation coefficient r = 0.08824, **p = 0.0083- analyzed by simple linear regression test). The red solid line is the fitted regression line, and the green shaded area corresponds to a range of standard aPTT values. The Kaplan–Meier survivor functions according to (**F**) aPTT, **G** PT, **H** INR and **I** Fibrinogen levels in patients. Log-rank tests between a normal aPTT and a shorter aPTT, PT and INR are shown (lowest quartile), and for fibrinogen the log-rank test is between normal and higher values (highest quartile are shown).

3 weeks after injection by BLI, confirming the effectiveness of the antiplatelet antibody in each experimental setting by counting platelets prior to and during the homing assay.

Isolation of platelets

Platelets were isolated as described previously⁹⁰. Briefly, female and male DIO mice were anesthetized with ketamine (100 mg/kg) and xylazine (10 mg/kg), and whole blood was drawn by cardiac puncture using a syringe containing acid citrate dextrose (1 volume of

anticoagulant/9 volumes of blood). Blood was mixed with 1 volume of modified HEPES-Tyrode's buffer (140 mM NaCl, 2 mM KCl, 12 mM NaHCO₃, 0.3 mM NaH₂PO₄, 1 mM MgCl₂, 5.5 mM glucose, 5 mM HEPES, 2 mM EGTA, and 0.035% BSA, pH 6.7) and it was centrifuged at 150 g for 2 minutes to obtain platelets or platelet-rich plasma (PRP). Prostaglandin E1 (PGE1, 5 nM: Millipore Sigma) was then added and the platelets were pelleted by centrifugation at 1500 g for 4 minutes at 37 °C. Platelet pellets were finally suspended in modified HEPES-Tyrode's buffer without EGTA and BSA (pH 7.4) but in the presence of 0.02

U/ml apyrase (grade VII: Millipore Sigma). Platelets were counted and pooled at the density necessary for each experiment.

In vitro aggregation studies

For murine platelet aggregation studies, washed platelets isolated from female and male mice, and female DIO mice ($250 \,\mu$ l of 5×10^8 platelets/ml) were used. Optical platelet aggregation experiments were monitored by turbidimetry using an aggregometer (Chrono-log 490 Optical Aggregometer) with continuous stirring at 1200 rpm at 37 °C. A final concentration of 0.5 IU/ml thrombin and $5 \,\mu$ g/ml collagen (Chrono-log Corporation) was used as an agonist for the aggregation studies.

Analysis of platelet α -granule release activation by flow cytometry

To analyze αIIbβ3 integrin activation (GPIIb/IIIa, CD41/CD61) in murine platelets isolated from male mice after DIO, washed platelets (100 µl of 1×10⁶ platelets/ml) were activated with 0.05 IU/ml thrombin or left untreated, and analyzed by flow cytometry after incubating them with PE-labeled anti- GPIIb/IIIa (Emfret, clone JON/A) and anti-CD62-P FITC antibodies (Emfret, clone Wug.E9) for 15 minutes at RT. Reactions were stopped by adding 400 µl PBS and the samples were analyzed within 30 minutes on a FACS CANTO II (BD, San Jose CA) and using FloJo v10 (BD). All antibody details and dilutions are available in Suppl. Table 1. Pools of platelets from 3 mice per diet were used in each condition. Ex vivo fibronectin binding and uptake assays were performed following the protocol described previously for fibrinogen adapted with some modifications⁹¹, briefly washed platelets $(1.0 \times 10^7/\text{mL})$ were incubated with FITC-FN (0.15 mg/mL, Cytoskeleton, Inc.) at 37 °C for the indicated times. The platelets were fixed with 2% paraformaldehyde and analyzed by FACS. To study fibronectin uptake, platelets were fixed with 2% paraformaldehyde and analyzed by flow cytometry after addition of 0.04% trypan blue (Sigma). Pools of platelets from 3 mice per diet were used in each condition.

Analysis of signaling pathways in platelets

Washed platelets isolated from male DIO mice (250 μ l of 5 × 10⁸ platelets/ml) were activated with 0.05 IU/ml thrombin (Chrono-log Corporation) and incubated at 37 °C for different times: untreated, 0 min; activated 15 and 30 seconds, and 3, 7 or 15 min. Subsequently, 250 μ l 2× RIPA lysis buffer was added: 100 mM Tris-HCl [pH 8.0], 0.2% SDS, 2% NP-40, 1% sodium deoxycholate, supplemented with a mixture of protease and phosphatase inhibitors (PMSF 2 mM, Leupeptine 10 μ g/ml, NaF 50 mM, Aprotinin 5 μ g/ml, Sodium Orthovanadate 0.3 mM). Signaling pathways were analyzed in immunoblots of total protein extracts from washed platelets probed with the antibodies indicated (Suppl. Table 1). Pools of platelets from 3 mice per diet were used in each condition. When indicated, platelets were pretreated with TNF α (1 μ g/ml, Peprotech) for 5, 15 and 30 minutes at 37 °C before activation.

Platelet dense granule secretion assay

The release of ATP stored in platelet dense granules was measured as light output generated following an ATP-luciferin-luciferase reaction. The assay was carried out as described previously 92 . Briefly, washed platelets isolated from male DIO mice $(5\times10^8/\text{mL},\,180\,\mu\text{L})$ were incubated in a white Corning Costar flat bottom 96-well plate for 5 minutes at 37 °C on an orbital shake. Platelet agonizts (Thrombin 0.01 IU/ml) and CaCcl $_2$ (2 mM) were then added, and platelets were activated for 30 seconds (s) at 37 °C on an orbital shaker. ATP standards were assayed in the same plate. Finally, 50 μL of the Chronolume detection reagent (Chrono-Log Corporation, Havertown, PA, USA) was added to each well and the corresponding luminescence emitted was measured (in arbitrary units) for 3 s in a multiple-well Reader (ClarioStarPlus. Luminiscence) following a 1 s delay. Pools of platelets from 3 mice per diet were used in each condition. The assay was performed in triplicate on at least two independent experiments.

Platelet spreading assays

Spreading assays were performed as described previously⁹¹. In brief. Lab-Tek Chamber Slides (Nunc) were coated overnight at 4 °C with 100 µg/ml human fibrinogen (Millipore Sigma) in PBS [pH 8.0] and after washing with PBS, they were blocked for 2 hours at RT with heatdenatured BSA (5 mg/ml) and then washed again. Platelets isolated from male DIO mice (1×108 platelets/ml) were incubated on the fibrinogen-coated chambers and allowed to spread for 5, 15, 30 and 60 minutes at 37 °C in the presence of 0.01 IU/ml thrombin. Pools of platelets from 3 mice per diet were used in each condition. The chambers were then washed and the adhered platelets were fixed with paraformaldehyde (PFA, 4%) for 10 minutes. After washing again, the chambers were incubated with 100 mM glycine for 5 minutes, washed and then permeabilized with 0.2% Triton X-100 for 5 minutes. The plates were washed further, blocked for 30 minutes with 10% normal goat serum (NGS: Millipore Sigma) and then probed with an anti-αtubulin primary antibody, followed by the Alexa Fluor 488 goat antimouse secondary antibody. Phalloidin-Alexa Fluor 564 (A22283, ThermoFisher) was used to stain F-actin (T9026, Sigma) and images were acquired with a TCS SP5 X confocal microscope (Leica-Microsystems) equipped with AOBS, a HCX PLAN APO CS 63x/1.4 Oil Immersion, a HCX PLAN APO CS 100×/1.4 Oil Immersion objective and LAS AF v2.7.5 software. To quantify platelet morphology, at least 150 platelets per sample were measured using Fiji v2.1software.

Platelet adhesion assay

Adhesion assays were performed as described previously 93 . In brief, microplate wells coated with fibrinogen (Millipore Sigma) were blocked for 1 h at RT and washed with PBS before adding the platelets isolated from male DIO mice. The platelets (50 ul of 1×10^8 platelets/ml) were unactivated, or activated by exposing to thrombin (0.05 U/ml, final activity) for 20 to 60 min at RT, and had been washed four times with PBS before they were diluted in the phosphatase substrate solution (5 mM p-nitrophenyl phosphate). After a 1 hour incubation, 2 M NaOH was added and the resulting formation of p-nitrophenol was measured spectrophotometrically in Multi-well Clario Star Plus Reader at $\lambda = 405$ nm absorbance. The assay was performed in triplicate for at least two independent experiments.

Scanning electron microscopy

EO771 $(1.5\times10^5 \text{ tumor cells})$ were washed in serum free media prior incubation with platelet suspensions $(1.5\times10^6 \text{ platelets})$ at indicated concentrations. Purified platelets were incubated with EO771 tumor cells for 1 h at room temperature then fixed with 2.5% glutaraldehyde and 4% paraformaldehyde prepared in Milloning phosphate buffer for 4 h. Pools of platelets from 3 mice per diet were used in each condition. After washing in distilled water, samples were dehydrated in an ethanol series (30, 50, 70, 80, 90, 95 and 100% for 10 min each). The samples were dried in a critical point dryer (Leica EM CPD300; Leica Microsystems). A 10 nm gold layer was sputtered onto the surface of the samples. Image acquisition was performed at high resolution (20 kV) and $\times 3000$ –6000 magnification under an JEOL JSM 6400 scanning electron microscope.

Mouse XL Cytokine Assay

A commercially available antibody array kit (Proteome Profiler Mouse XL Cytokine Array, R & D Systems, ARY028) which was coated with 111 different cytokine antibodies in duplicate on a nitrocellulose membrane (dot blot) was used, following the manufacturer's instructions. This cytokine antibody array was used to determine the effects of platelets exposure on cytokine synthesis by EO771 cells compared with the analysis of adipose tissue-secreted soluble factors from ND and HFD-fed mice. The assay required 500 μL of cell culture supernatants (unstimulated and Platelet stimulated (1 × 10°). Pools of platelets from 3 mice per diet were used in each condition. Membrane images were

quantified, processing and analyzed using Fiji v2.1. software. Levels of cytokines were expressed and normalized against of the reference spots and relativized to the control condition (EO771 or ND secreted factors). Only the cytokines that showed similar expression patterns in both between the HFD conditions are shown.

Tumor cell adhesion to endothelial cells

HUVECs were grown to form a monolayer on gelatin-coated 6-well plates and activated by adding 100 µl of PKH26-labeled-platelets from male DIO mice (1×10⁸ platelets/ml) for 45 min. Pools of platelets from 3 mice per diet were used in each condition. Platelets were washed and 1x10⁵ EO771 cells were added to each well and allowed to adhere for 45 min. The cells were gently washed twice with medium and fixed in 4% PFA. When indicated, HUVECs were treated with an anti-FN1 blocking antibody (100 mg/ml) for 16 h (IST9, Abcam, ab6328). Images were acquired on a Thunder Imaging System (Leica-Microsystems) equipped with a 5X/0.15 Air Objective, a 8-LED light source, a DFC9000GTC camera and LAS-X v3.9.1 software. Random fields were obtained and analyzed with Fiji v.2.1 software.

In vitro transendothelial migration assay (TEM)

TEM assays were set up as described previously¹0. Briefly, endothelial cells (HUVEC or HMEC) were seeded in Transwell chambers (8 μm, 24-well format) at a density 100,000 cells/well and allowed to form monolayers. Endothelial monolayers were pre-treated with platelets isolated from female DIO mice (500,000 platelets/well, 45 min exposure). Pools of platelets from 3 mice per diet were used in each condition. BC cells were labeled with the Vybrant CFDA SE Cell Tracer (Invitrogen) to differentiate them from endothelial cells, they were seeded in the upper chamber (4000 cells/well, Py230 or EO771 cells) and then allowed to migrate across the endothelial monolayer to the underside of the Transwell chamber over 24 h along a 0-2% FBS gradient. The cells that migrated to the underside of the Transwell chamber were quantified under a fluorescent microscope using a 10x objective.

Immunoblotting

Western blots were performed on 30-60 μ g of total protein extract from murine platelets and RIPA whole cell lysates, resolved by SDS-PAGE. Membranes were blocked for 1 hour at RT with 5% (w/v) non-fat milk in TBS-T (50 mM Tris-Cl, 100 mM NaCl, 0.1% Tween-20, pH 7.4) and probed overnight at 4 °C with the antibodies indicated (Suppl. Table 1). The membranes were then rinsed 3 times with TBS-T and incubated with the secondary conjugated antibodies. Signals were detected using the ECL Western Blotting Substrate kit (GE Healthcare) or the Odyssey CLX system (Licor).

Histological studies

Tissue samples were fixed in 10% neutral buffered formalin (4% formaldehyde in solution), paraffin-embedded, and 3 µm sections were mounted on TOMO®slides and dried overnight. For different staining methods, slides were deparaffinized in xylene and re-hydrated through a series of graded ethanols until they reached water. Consecutive sections were H&E stained and different immunohistochemistry reactions were carried out in an automated immunostaining platform (Discovery XT-ULTRA, Ventana-Roche). Antigen retrieval was performed with the appropriate pH buffer (CC1: Ventana, Roche) and endogenous peroxidases were blocked with hydrogen peroxide (3%). The slides were then incubated with the appropriate primary antibody (anti-P53, anti-fibronectin or anti-P-selectin: Suppl. Table 1) and then with the corresponding horseradish peroxidase conjugated secondary antibodies: anti-rat (Vector) and OmniMap anti-Rabbit visualization systems (Ventana, Roche). The immunohistochemical reaction was developed using 3, 30-diaminobenzidine tetrahydrochloride (DAB: ChromoMap DAB, Ventana, Roche) and the nuclei were counterstained with hematoxylin. Finally, the slides were dehydrated, cleared and mounted in a permanent mounting medium for microscopy. Positive control sections known to be positive for the primary antibody were included in each staining run. The images from the whole slides were acquired on a slide scanner (AxioScan Z1, Zeiss) and captured with the Zen Blue Software (V3.1 Zeiss).

Immunofluorescence

Cells were blocked with 4% PFA for 20 min and after three washes with PBS, the sections were incubated for 15 min with PBS containing 0.2% Triton X-100. Samples were blocked for 1 h at RT with PBS containing 1% BSA, 5% donkey serum and 0.05% Triton X-100. After three washes, the tissues were probed with the primary antibodies at 4 °C overnight (see Suppl. Table 1) and after another three washes, they were incubated for 1 h with the Alexa Fluor secondary antibodies (diluted 1:500: Molecular Probes) and washed again. The samples were mounted with Prolong DAPI (Thermo), images were obtained using a TCS-SP8 STED 3X confocal microscope (Leica-Microsystems) equiped with a 63X/NA1.4 oil immersion objective, AFC, AOBS, a tunable white laser and LAS-X software v3.7.5. Images were analyzed with Fiji v2.1 software.

Isolation lung endothelial cells

Mouse lung endothelial cells (MLECs) were obtained and cultured as described previously^{94,95}. Briefly, lungs from male DIO mice were excised, disaggregated and digested in 0.1% collagenase (Gibco) for 1 h at 37 °C. The cell suspensions was seeded onto plates coated with 10 μg/ml fibronectin (Sigma), 10 μg/ml collagen I (PureCol) and 0.1% gelatin (Sigma). After attachment, the cells were negatively selected with an anti-CD16/CD32 mAb (BD Biosciences, 553141) coupled to magnetic beads (Dynal, Invitrogen, 11035) and then positively selected with anti-ICAM-2 (BD Biosciences, 553325) coupled to magnetic beads. The cells recovered were seeded onto plates coated with 10 µg/ml collagen I and left to reach confluency after a further 7 days. The cell suspension was stained with CD45-PB (Invitrogen, MCD4528), CD31-APC (BD Biosciences, 551262) and 7-AAD Viability Dve (Invitrogen. A1310). Doublets and dead cells were gated prior to FACS sorting in a FACS ARIA IIu (BD), and viable CD45⁻ CD31⁺ ECs were sorted into collecting medium containing 10% FBS (Thermo Fisher Scientific) and immediately frozen to isolate RNA (all the details on the antibodies and their dilutions are available in Suppl. Table 1).

RNA extraction, sequencing and data analysis

Total RNA was extracted from the cells using the TRIzol Reagent (Invitrogen). After recovering the aqueous phase using chloroform, DNase treatment and further purification was performed with the RNeasy Micro kit (Qiagen), following the manufacturer's instructions. Subsequently, 500 cells per sample were processed with the "NEBNext Single Cell/Low Input RNA Library Prep" kit (NEB #E6420), according to the manufacturer's instructions. Briefly, extracts obtained by suspending the sample in cell lysis buffer were subjected to oligo(dT) primed reverse transcription in a template switching reaction. Double stranded cDNA was then produced by limited-cycle PCR, and sequencing libraries were completed with the "NEBNext Ultra II FS DNA Library Prep Kit for Illumina" (NEB #E7805) and analyzed on an Illumina NextSeq 550 (with v2.5 reagent kits). Single-end 85 bp reads were obtained, their clontech adapters were removed with Cutadapt (https://cutadapt.readthedocs.io/en/stable/), subsequently removing the last 15 bp from the reads, and they were then analyzed in the nextpresso pipeline⁹⁶: sequencing quality was checked with FastQC v0.11.7 (http://www.bioinformatics.babraham.ac.uk/projects/fastqc/); reads were aligned to the mouse reference genome (GRCm38) with TopHat-2.0.10⁹⁷, using Bowtie 1.0.0⁹⁸ and Samtools 0.1.19⁹⁹, and allowing three mismatches and twenty multi-hits; read counts were obtained with HTSeq-count v0.6.1 100 , using the mouse gene annotation from GENCODE (encode.vM20.GRCm38.Ensembl95)¹⁰¹; differential expression was established with DESeq2¹⁰², using a 0.05 FDR; GSEAPreranked¹⁰³ was used to perform gene set enrichment for several gene signatures on a pre-ranked gene list, setting 1,000 gene set permutations. Only those gene sets with significant enrichment (FDR q-value < 0.25) were considered.

Proteomics analysis

Platelets from male DIO mice were lysed in 7 M urea and 2 M thiourea, digested with trypsin using the standard FASP protocol and labeled using the iTRAQ® reagent 8-plex. Pools of platelets from 3 mice per diet were used in each condition For whole proteome analysis, peptides were fractionated using an online HpH reverse-phase HPLC system and then, concatenated into 15 fractions. Samples were analyzed by LC-MS/MS using an Impact Mass Spectrometer (Bruker) and the Raw files obtained were analyzed with MaxQuant against a mouse protein database. Statistical analysis was achieved with Prostar. To integrate the RNA-seq performed on CD45°, CD31° MLECS and the proteomic profile of platelets isolated from ND (N = 3) and HFD (N = 3) male mice, 2916 genes in common RNA-protein pairs were considered. Co-regulated pairs were FDR < 0.05 (colored), 5 above the FC cut-off (in solid color) applying a protein fold change >0.25 or <-0.25.

Intravital imaging of the lung

Intravital microscopy of the lung was performed as reported elsewhere¹⁰⁴. Briefly, male DIO mice were anesthetized and ventilated mechanically through the trachea using a small-animal ventilator (model 687: Harvard Apparatus). A right lateral thoracotomy was performed and the lung was positioned under the window of a custombuilt fixation device, applying a mild vacuum to hold the lung in position during microscopy. To visualize platelets, anti-CD41-PE was injected intravenously (1 µg/mouse), and the lungs were then analyzed 10 min after the mice were injected with an anti-CD41-PE-antibody and 1x10⁵ EO771-GFP cells. Kinetic parameters were quantified, such as the Tumor-Platelet Aggregation index (Fig. 4G), quantifying the platelets in the tumor cell area and those in the surrounding region. A ratio between the interacting platelets (closer) and the total platelets in the area (both interacting and non-interacting) was then calculated (see Suppl. Figure 3E for more details). We calculated the platelet accumulation around tumor cells and the same area measured in a different region (random location) without green cells to verify the specificity of the interactions. Intravital experiments were performed on a TCS SP5 confocal microscope (Leica-Microsystems) equipped with a 20x/NA 0.7 dry objective, an AOBS and a temperature controller driven by the LAS AF v2.6 software, and Z-stack time lapse videos were obtained and analyzed using an ImageJ macro¹⁰⁵. The algorithm developed involved: first finding the tumor cell in each frame and its segmentation into the green channel; this region of interest is dilated to obtain a new area around the cell (surrounding region); subsequently, the platelet area is segmented into the red channel; and finally, the total area is measured and the number of particles in each region of interest was assessed (tumor cells and surrounding region). In addition, other measures were calculated, like the segmented area of the platelets in the full frame and the size of the tumor cell. These measures were studied and analyzed using SPSS and Microsoft Excel to obtain the results shown here.

Statistics and reproducibility

The sample size for in vitro and in vivo experiments was selected based on pilot studies. Animals were randomly allocated for dietary studies and for studies involving tumor cell injection. For all other experiments, no specific randomization method was followed as this was irrelevant for the in vitro assays. Researchers were blind to the final outcome assessment in the mouse experiments but not to the allocation or treatment of the mice in the experiments. For the remaining in vitro experiments, researchers were not blinded but the

experiments were performed by different individuals. Error bars in the graphical data represent the mean \pm s.d. unless otherwise specified. For in vivo and in vitro assays, the number of independent experiments and biological replicates are indicated in the figure legends. Statistical significance was determined using GraphPad Prism software v.9.1.0, applying a two-tailed unpaired or paired Student's t-tests, one-way or two-way ANOVA, or non-parametric tests as appropriate. For human studies, Pearson's correlation was assessed for bivariate correlations between the BMI and each coagulation test parameter. Survival analyzes were carried out with Kaplan-Meier estimates and LogRank tests. Multivariate analyzes were performed according to the Cox's proportionate hazards methods. All tests were two-sided and a *P*-value cut-off of 0.05 was deemed statistically significant. All these tests were performed with the SPSS V.11 software package.

Reporting summary

Further information on research design is available in the Nature Portfolio Reporting Summary linked to this article.

Data availability

Raw data from RNA sequencing and mass spectrometry analysis are publicly available. The RNA analysis data has been deposited in the GEO database: accession No. GSE237839. Mass spectrometry raw data raw data is deposited in the ProteomeXchange Consortium via the PRIDE partner repository with the dataset identifier PXD051176. All the data and materials referred to in the main text or the supplementary materials are available upon request. Source data are provided with this paper.

References

- Massague, J. & Ganesh, K. Metastasis-initiating cells and ecosystems. Cancer Discov. 11, 971–994 (2021).
- Lambert, A. W., Pattabiraman, D. R. & Weinberg, R. A. Emerging biological principles of metastasis. Cell 168, 670–691 (2017).
- de Visser, K. E. & Joyce, J. A. The evolving tumor microenvironment: from cancer initiation to metastatic outgrowth. *Cancer Cell* 41, 374–403 (2023).
- Rubio-Jurado, B. et al. Obesity, thrombotic risk, and inflammation in cancer. Adv. Clin. Chem. 85, 71–89 (2018).
- Calle, E. E., Rodriguez, C., Walker-Thurmond, K. & Thun, M. J. Overweight, obesity, and mortality from cancer in a prospectively studied cohort of U.S. adults. N. Engl. J. Med 348, 1625–1638 (2003).
- Petrelli, F. et al. Association of obesity with survival outcomes in patients with cancer: a systematic review and meta-analysis. JAMA Netw. Open 4, e213520 (2021).
- Harborg, S. et al. Overweight and prognosis in triple-negative breast cancer patients: a systematic review and meta-analysis. NPJ Breast Cancer 7, 119 (2021).
- McDowell S. A. C., et al. Obesity alters monocyte developmental trajectories to enhance metastasis. J Exp Med 220, e20220509 (2023).
- Quail, D. F. et al. Obesity alters the lung myeloid cell landscape to enhance breast cancer metastasis through IL5 and GM-CSF. Nat. Cell Biol. 19, 974–987 (2017).
- McDowell, S. A. C. et al. Neutrophil oxidative stress mediates obesity-associated vascular dysfunction and metastatic transmigration. Nat. Cancer 2, 545–562 (2021).
- 11. Ellulu, M. S., Patimah, I., Khaza'ai, H., Rahmat, A. & Abed, Y. Obesity and inflammation: the linking mechanism and the complications. *Arch. Med Sci.* **13**, 851–863 (2017).
- Henning, R. J. Obesity and obesity-induced inflammatory disease contribute to atherosclerosis: a review of the pathophysiology and treatment of obesity. Am. J. Cardiovasc Dis. 11, 504–529 (2021).

- Falanga, A., Russo, L., Milesi, V. & Vignoli, A. Mechanisms and risk factors of thrombosis in cancer. *Crit. Rev. Oncol. Hematol.* 118, 79–83 (2017).
- Erpenbeck, L. & Schon, M. P. Deadly allies: the fatal interplay between platelets and metastasizing cancer cells. *Blood* 115, 3427–3436 (2010).
- Braun, A., Anders, H. J., Gudermann, T. & Mammadova-Bach, E. Platelet-cancer interplay: molecular mechanisms and new therapeutic avenues. Front Oncol. 11, 665534 (2021).
- Xu, X. R. et al. Platelets are versatile cells: New discoveries in hemostasis, thrombosis, immune responses, tumor metastasis and beyond. Crit. Rev. Clin. Lab Sci. 53, 409–430 (2016).
- Nieswandt, B., Hafner, M., Echtenacher, B. & Mannel, D. N. Lysis of tumor cells by natural killer cells in mice is impeded by platelets. Cancer Res 59, 1295–1300 (1999).
- Palumbo, J. S. et al. Platelets and fibrin(ogen) increase metastatic potential by impeding natural killer cell-mediated elimination of tumor cells. *Blood* 105, 178–185 (2005).
- Gay, L. J. & Felding-Habermann, B. Contribution of platelets to tumour metastasis. *Nat. Rev. Cancer* 11, 123–134 (2011).
- Labelle, M., Begum, S. & Hynes, R. O. Platelets guide the formation of early metastatic niches. *Proc. Natl Acad. Sci. USA* 111, E3053–E3061 (2014).
- Labelle, M. & Hynes, R. O. The initial hours of metastasis: the importance of cooperative host-tumor cell interactions during hematogenous dissemination. *Cancer Discov.* 2, 1091–1099 (2012).
- Peinado, H. et al. Pre-metastatic niches: organ-specific homes for metastases. Nat. Rev. Cancer 17, 302–317 (2017).
- Coller, B. S. & Shattil, S. J. The GPIIb/IIIa (integrin alphallbbeta3) odyssey: a technology-driven saga of a receptor with twists, turns, and even a bend. *Blood* 112, 3011–3025 (2008).
- Shattil, S. J., Kim, C. & Ginsberg, M. H. The final steps of integrin activation: the end game. *Nat. Rev. Mol. Cell Biol.* 11, 288–300 (2010).
- Shattil, S. J. & Newman, P. J. Integrins: dynamic scaffolds for adhesion and signaling in platelets. *Blood* 104, 1606–1615 (2004).
- 26. Wu, Y. et al. The Tyrosine Kinase c-Src Specifically Binds to the Active Integrin alphallbbeta3 to Initiate Outside-in Signaling in Platelets. *J. Biol. Chem.* **290**, 15825–15834 (2015).
- Shen, B. et al. A directional switch of integrin signalling and a new anti-thrombotic strategy. *Nature* 503, 131–135 (2013).
- Konopatskaya, O. et al. PKCalpha regulates platelet granule secretion and thrombus formation in mice. J. Clin. Invest 119, 399–407 (2009).
- Yoshioka, A. et al. Identification of protein kinase Calpha as an essential, but not sufficient, cytosolic factor for Ca2+-induced alpha- and dense-core granule secretion in platelets. *J. Biol.* Chem. 276, 39379–39385 (2001).
- Chen, J. et al. Impaired platelet responses to thrombin and collagen in AKT-1-deficient mice. *Blood* 104, 1703–1710 (2004).
- Mazharian, A., Thomas, S. G., Dhanjal, T. S., Buckley, C. D. & Watson, S. P. Critical role of Src-Syk-PLCgamma2 signaling in megakaryocyte migration and thrombopoiesis. *Blood* 116, 793–800 (2010).
- 32. Levy-Toledano, S. Platelet signal transduction pathways: could we organize them into a 'hierarchy'? *Haemostasis* **29**, 4–15 (1999).
- Levy-Toledano, S. et al. Phosphorylation and dephosphorylation mechanisms in platelet function: a tightly regulated balance. Thromb. Haemost. 78, 226–233 (1997).
- 34. Kwaifa I. K., Bahari H., Yong Y. K., Noor S. M. Endothelial dysfunction in obesity-induced inflammation: molecular mechanisms and clinical implications. *Biomolecules* **10**, 291 (2020).
- 35. Ingalls, A. M., Dickie, M. M. & Snell, G. D. Obese, a new mutation in the house mouse. *J. Hered.* **41**, 317–318 (1950).

- Coleman, D. L. & Hummel, K. P. The influence of genetic background on the expression of the obese (Ob) gene in the mouse. *Diabetologia* 9, 287–293 (1973).
- Kaplan, R. N. et al. VEGFR1-positive haematopoietic bone marrow progenitors initiate the pre-metastatic niche. *Nature* 438, 820–827 (2005).
- 38. Ni, H., Papalia, J. M., Degen, J. L. & Wagner, D. D. Control of thrombus embolization and fibronectin internalization by integrin alpha IIb beta 3 engagement of the fibrinogen gamma chain. *Blood* **102**, 3609–3614 (2003).
- Hotamisligil, G. S., Shargill, N. S. & Spiegelman, B. M. Adipose expression of tumor necrosis factor-alpha: direct role in obesitylinked insulin resistance. Science 259, 87–91 (1993).
- Johnstone, C. N. et al. Functional and molecular characterisation of EO771.LMB tumours, a new C57BL/6-mouse-derived model of spontaneously metastatic mammary cancer. *Dis. Model Mech.* 8, 237–251 (2015).
- Zou, L., Cao, S., Kang, N., Huebert, R. C. & Shah, V. H. Fibronectin induces endothelial cell migration through beta1 integrin and Srcdependent phosphorylation of fibroblast growth factor receptor-1 at tyrosines 653/654 and 766. J. Biol. Chem. 287, 7190–7202 (2012).
- 42. Pulous, F. E., Grimsley-Myers, C. M., Kansal, S., Kowalczyk, A. P. & Petrich, B. G. Talin-dependent integrin activation regulates vecadherin localization and endothelial cell barrier function. *Circ. Res* **124**, 891–903 (2019).
- 43. Hu, G., Place, A. T. & Minshall, R. D. Regulation of endothelial permeability by Src kinase signaling: vascular leakage versus transcellular transport of drugs and macromolecules. *Chem. Biol. Interact.* **171**, 177–189 (2008).
- Li, Z., Delaney, M. K., O'Brien, K. A. & Du, X. Signaling during platelet adhesion and activation. *Arterioscler Thromb. Vasc. Biol.* 30, 2341–2349 (2010).
- Sechler, J. L., Corbett, S. A. & Schwarzbauer, J. E. Modulatory roles for integrin activation and the synergy site of fibronectin during matrix assembly. Mol. Biol. Cell 8, 2563–2573 (1997).
- 46. Schumacher S., et al. Structural insights into integrin alpha(5) beta(1) opening by fibronectin ligand. Sci. Adv. 7, eabe9716 (2021).
- Ju, J. A. et al. Hypoxia Selectively enhances integrin alpha(5) beta(1) receptor expression in breast cancer to promote metastasis. Mol. Cancer Res 15, 723–734 (2017).
- Varner, J. A., Emerson, D. A. & Juliano, R. L. Integrin alpha 5 beta 1 expression negatively regulates cell growth: reversal by attachment to fibronectin. *Mol. Biol. Cell* 6, 725–740 (1995).
- Pantano, F. et al. Integrin alpha5 in human breast cancer is a mediator of bone metastasis and a therapeutic target for the treatment of osteolytic lesions. Oncogene 40, 1284–1299 (2021).
- Schimmel L., et al. c-Src controls stability of sprouting blood vessels in the developing retina independently of cell-cell adhesion through focal adhesion assembly. *Development* 147, dev185405 (2020).
- Bergmeier, W., Rackebrandt, K., Schroder, W., Zirngibl, H. & Nieswandt, B. Structural and functional characterization of the mouse von Willebrand factor receptor GPIb-IX with novel monoclonal antibodies. *Blood* 95, 886–893 (2000).
- Dent, R. et al. Triple-negative breast cancer: clinical features and patterns of recurrence. Clin. Cancer Res 13, 4429–4434 (2007).
- Menter, D. G. et al. Platelets and cancer: a casual or causal relationship: revisited. Cancer Metastasis Rev. 33, 231–269 (2014).
- Blokhin, I. O. & Lentz, S. R. Mechanisms of thrombosis in obesity.
 Curr. Opin. Hematol. 20, 437–444 (2013).
- 55. Badimon, L., Hernandez Vera, R. & Vilahur, G. Atherothrombotic risk in obesity. *Hamostaseologie* **33**, 259–268 (2013).
- Senis, Y. A., Mazharian, A. & Mori, J. Src family kinases: at the forefront of platelet activation. *Blood* 124, 2013–2024 (2014).

- Kim, M. P., Park, S. I., Kopetz, S. & Gallick, G. E. Src family kinases as mediators of endothelial permeability: effects on inflammation and metastasis. Cell Tissue Res 335, 249–259 (2009).
- 58. Petrich, B. G. Talin-dependent integrin signalling in vivo. *Thromb. Haemost.* **101**, 1020–1024 (2009).
- Hynes, R. O. Integrins: a family of cell surface receptors. Cell 48, 549–554 (1987).
- 60. De Kock L., Freson K. The (Patho)biology of SRC kinase in platelets and megakaryocytes. *Medicina (Kaunas)* **56**, 633 (2020).
- 61. Harper, M. T. & Poole, A. W. Diverse functions of protein kinase C isoforms in platelet activation and thrombus formation. *J. Thromb. Haemost.* **8**, 454–462 (2010).
- Murphy J. M., Jeong K., Lim S. S. FAK family kinases in vascular diseases. *Int. J. Mol. Sci.* 21, 3630 (2020).
- 63. Yau, J. W., Teoh, H. & Verma, S. Endothelial cell control of thrombosis. *BMC Cardiovasc Disord.* **15**, 130 (2015).
- Bondareva, O. et al. Single-cell profiling of vascular endothelial cells reveals progressive organ-specific vulnerabilities during obesity. Nat. Metab. 4, 1591–1610 (2022).
- 65. Neubauer, K. & Zieger, B. Endothelial cells and coagulation. *Cell Tissue Res* **387**, 391–398 (2022).
- 66. Bergmeier W., Hynes R. O. Extracellular matrix proteins in hemostasis and thrombosis. *Cold Spring Harb. Perspect Biol.* **4**, a005132 (2012).
- 67. Cloutier, N. et al. Platelets can enhance vascular permeability. *Blood* **120**, 1334–1343 (2012).
- To, W. S. & Midwood, K. S. Plasma and cellular fibronectin: distinct and independent functions during tissue repair. Fibrogenes. Tissue Repair 4, 21 (2011).
- Wang, Y. et al. Plasma fibronectin supports hemostasis and regulates thrombosis. J. Clin. Invest 124, 4281–4293 (2014).
- 70. Maurer, E. et al. Fibrillar cellular fibronectin supports efficient platelet aggregation and procoagulant activity. *Thromb. Haemost.* **114**, 1175–1188 (2015).
- Cho, J. & Mosher, D. F. Enhancement of thrombogenesis by plasma fibronectin cross-linked to fibrin and assembled in platelet thrombi. *Blood* 107, 3555–3563 (2006).
- Prakash, P., Kulkarni, P. P., Lentz, S. R. & Chauhan, A. K. Cellular fibronectin containing extra domain A promotes arterial thrombosis in mice through platelet Toll-like receptor 4. *Blood* 125, 3164–3172 (2015).
- Malik, G. et al. Plasma fibronectin promotes lung metastasis by contributions to fibrin clots and tumor cell invasion. *Cancer Res* 70, 4327–4334 (2010).
- Kanters, S. D. et al. Plasma levels of cellular fibronectin in diabetes. *Diab. Care* 24, 323–327 (2001).
- Dhanesha, N., Jain, M., Doddapattar, P., Undas, A. & Chauhan, A. K. Cellular fibronectin promotes deep vein thrombosis in diet-induced obese mice. J. Thromb. Haemost. 19, 814–821 (2021).
- Yurdagul, A. Jr. et al. alpha5beta1 integrin signaling mediates oxidized low-density lipoprotein-induced inflammation and early atherosclerosis. Arterioscler Thromb. Vasc. Biol. 34, 1362–1373 (2014).
- Green, J., Yurdagul, A. Jr., McInnis, M. C., Albert, P. & Orr, A. W. Flow patterns regulate hyperglycemia-induced subendothelial matrix remodeling during early atherogenesis. *Atherosclerosis* 232, 277–284 (2014).
- Feaver, R. E., Gelfand, B. D., Wang, C., Schwartz, M. A. & Blackman, B. R. Atheroprone hemodynamics regulate fibronectin deposition to create positive feedback that sustains endothelial inflammation. Circ. Res 106, 1703–1711 (2010).
- Schaffner, F., Ray, A. M. & Dontenwill, M. Integrin alpha5beta1, the fibronectin receptor, as a pertinent therapeutic target in solid tumors. *Cancers (Basel)* 5, 27–47 (2013).

- Bousquenaud, M., Fico, F., Solinas, G., Ruegg, C. & Santamaria-Martinez, A. Obesity promotes the expansion of metastasisinitiating cells in breast cancer. *Breast Cancer Res* 20, 104 (2018).
- 81. Foss, A., Munoz-Sagredo, L., Sleeman, J. & Thiele, W. The contribution of platelets to intravascular arrest, extravasation, and outgrowth of disseminated tumor cells. *Clin. Exp. Metastasis* **37**, 47–67 (2020).
- 82. Lickert, S. et al. Platelets drive fibronectin fibrillogenesis using integrin alphalibbeta3. Sci. Adv. 8, eabj8331 (2022).
- 83. Kim, Y. J., Borsig, L., Varki, N. M. & Varki, A. P-selectin deficiency attenuates tumor growth and metastasis. *Proc. Natl Acad. Sci. USA* **95**, 9325–9330 (1998).
- Borsig, L. et al. Heparin and cancer revisited: mechanistic connections involving platelets, P-selectin, carcinoma mucins, and tumor metastasis. Proc. Natl Acad. Sci. USA 98, 3352–3357 (2001).
- 85. Garcia-Leon, M. J. et al. Platelets favor the outgrowth of established metastases. *Nat. Commun.* **15**, 3297 (2024).
- Lake, B., Damery, S. & Jolly, K. Effectiveness of weight loss interventions in breast cancer survivors: a systematic review of reviews. *BMJ Open* 12, e062288 (2022).
- 87. Bian, X. et al. Roles of platelets in tumor invasion and metastasis: a review. *Heliyon* **8**, e12072 (2022).
- Lucotti, S. et al. Aspirin blocks formation of metastatic intravascular niches by inhibiting platelet-derived COX-1/thromboxane A2. J. Clin. Invest 129, 1845–1862 (2019).
- 89. Lucotti, S. & Muschel, R. J. Platelets and metastasis: new implications of an old interplay. *Front Oncol.* **10**, 1350 (2020).
- Prevost, N., Kato, H., Bodin, L. & Shattil, S. J. Platelet integrin adhesive functions and signaling. *Methods Enzymol.* 426, 103–115 (2007).
- Hurtado, B. et al. Thrombocytopenia-associated mutations in Ser/ Thr kinase MASTL deregulate actin cytoskeletal dynamics in platelets. J. Clin. Invest 128, 5351–5367 (2018).
- Mitrugno, A., Williams, D., Kerrigan, S. W. & Moran, N. A novel and essential role for FcgammaRIIa in cancer cell-induced platelet activation. *Blood* 123, 249–260 (2014).
- 93. Bellavite, P. et al. A colorimetric method for the measurement of platelet adhesion in microtiter plates. *Anal. Biochem* **216**, 444–450 (1994).
- Oblander, S. A. et al. Distinctive functions of membrane type 1 matrix-metalloprotease (MT1-MMP or MMP-14) in lung and submandibular gland development are independent of its role in pro-MMP-2 activation. *Dev. Biol.* 277, 255–269 (2005).
- Esteban, S. et al. Endothelial MT1-MMP targeting limits intussusceptive angiogenesis and colitis via TSP1/nitric oxide axis. EMBO Mol. Med 12, e10862 (2020).
- Graña, O., Rubio-Camarillo, M., Fdez-Riverola, F., Pisano, D. & Glez-Peña, D. Nextpresso: next generation sequencing expression analysis pipeline. *Curr. Bioinforma.* 13, 583–591 (2018).
- Trapnell, C. et al. Differential gene and transcript expression analysis of RNA-seq experiments with TopHat and Cufflinks. Nat. Protoc. 7, 562–578 (2012).
- 98. Langmead, B., Trapnell, C., Pop, M. & Salzberg, S. L. Ultrafast and memory-efficient alignment of short DNA sequences to the human genome. *Genome Biol.* **10**, R25 (2009).
- 99. Li, H. et al. The Sequence Alignment/Map format and SAMtools. *Bioinformatics* **25**, 2078–2079 (2009).
- Frankish, A. et al. Gencode 2021. Nucleic Acids Res 49, D916–D923 (2021).
- Anders, S., Pyl, P. T. & Huber, W. HTSeq-a Python framework to work with high-throughput sequencing data. *Bioinformatics* 31, 166–169 (2015).
- Love, M. I., Huber, W. & Anders, S. Moderated estimation of fold change and dispersion for RNA-seq data with DESeq2. *Genome Biol.* 15, 550 (2014).

- Subramanian, A. et al. Gene set enrichment analysis: a knowledgebased approach for interpreting genome-wide expression profiles. Proc. Natl Acad. Sci. USA 102, 15545–15550 (2005).
- Adrover, J. M. et al. Programmed 'disarming' of the neutrophil proteome reduces the magnitude of inflammation. *Nat. Immunol.* 21, 135–144 (2020).
- Schneider, C. A., Rasband, W. S. & Eliceiri, K. W. NIH Image to ImageJ: 25 years of image analysis. *Nat. Methods* 9, 671–675 (2012).

Acknowledgements

This work was supported by the Worldwide Cancer Research UK (24-0197, 16-1244), Agencia Estatal de Investigación/Ministerio de Ciencia e Innovación (AEI/MCIN: PID2020-118558RB-I00/AEI/10.13039/ 501100011033), WHRI-ACADEMY, a COFUND of Marie Curie action (WHRI-309), Fundación Bancaria "la Caixa" (HR18-00256) granted to HP. This work was also supported by grants from the Spanish National Research and Development Plan, Instituto de Salud Carlos III, and FEDER (PI20/01837 and PI23/01932 to S.R-P.); and AECC (AECC_Lab 2020) to S.R-P and ISCIII/FEDER (PI21/01641) to R.T-R. The CNIO is a certified Severo Ochoa Center of Excellence, supported by the Spanish Government through the Instituto de Salud Carlos III (ISCIII). We thank Drs. Cyrus Ghajar, Luuke Hawinkels and Inge Verbrugge for providing cell lines, and we are grateful to Beatriz Salinas (Hospital General Universitario Gregorio Marañon) for synthetizing the NIR-IF dextran. We also thank the CNIO Histopathology Unit for their technical support and Alicia Garcia Arroyo (Centro de Investigaciones Biologicas) for her help in isolating MLECs. Figures were partially created with Servier Medical Art (https://smart.servier.com/) and Adobe Illustrator 24.1.

Author contributions

M.H.-R., S.S.-R., V.S., M.P.-M., P.X.-E., S.A.C.M., M.S.M., R.T.-R., performed the experiments. M.H.-R., B.H., P.X., M.S.M., M.P.-M., G.M., O.G.-C., D.M. designed the experiments and analyzed the data. H.P., S.R.-P., L.M., D.M., D.Q., M.Q.-F. supervised the experiments. H.P. and M.H.-R. conceived the hypothesis, oversaw the project and wrote the paper. H.P. supervised all the work and obtained funding. All authors have read the final version of the manuscript and agree to its publication.

Competing interests

The authors declare no competing interests.

Additional information

Supplementary information The online version contains supplementary material available at https://doi.org/10.1038/s41467-025-57938-9.

Correspondence and requests for materials should be addressed to Héctor Peinado.

Peer review information *Nature Communications* thanks the anonymous reviewer(s) for their contribution to the peer review of this work. A peer review file is available.

Reprints and permissions information is available at http://www.nature.com/reprints

Publisher's note Springer Nature remains neutral with regard to jurisdictional claims in published maps and institutional affiliations.

Open Access This article is licensed under a Creative Commons Attribution-NonCommercial-NoDerivatives 4.0 International License, which permits any non-commercial use, sharing, distribution and reproduction in any medium or format, as long as you give appropriate credit to the original author(s) and the source, provide a link to the Creative Commons licence, and indicate if you modified the licensed material. You do not have permission under this licence to share adapted material derived from this article or parts of it. The images or other third party material in this article are included in the article's Creative Commons licence, unless indicated otherwise in a credit line to the material. If material is not included in the article's Creative Commons licence and your intended use is not permitted by statutory regulation or exceeds the permitted use, you will need to obtain permission directly from the copyright holder. To view a copy of this licence, visit https://creativecommons.org/licenses/by-nc-nd/4.0/.

© The Author(s) 2025

¹Microenvironment and Metastasis Laboratory, Molecular Oncology Programme, Spanish National Cancer Research Center (CNIO), Madrid, Spain. ²Cancer Cell Cycle Group, Preclinical & Translational Research Department, Vall d'Hebron Institute of Oncology (VHIO), Barcelona, Spain. ³Confocal Microscopy Unit, Biotechnology Programme, Spanish National Cancer Research Center (CNIO), Madrid, Spain. ⁴Proteomics Unit, Biotechnology Programme, Spanish National Cancer Research Center (CNIO), Madrid, Spain. ⁴Proteomics Unit, Biotechnology Programme, Spanish National Cancer Research Center (CNIO), Madrid, Spain. ⁵Rosalind and Morris Goodman Cancer Institute, McGill University, Montreal, Quebec, Canada. ⁶Division of Pediatrics, Department of Clinical Sciences, Lund University, Lund, Sweden. ⁷Lund Stem Cell Center (SCC), Lund University, Lund, Sweden. ⁸Department of Mathematics and Computer Science, University of La Rioja, La Rioja, Spain. ⁹Molecular Cytogenetics Unit, Human Cancer Genetics Programme, Spanish National Cancer Research Center (CNIO), Madrid, Spain. ¹⁰Division of Hematopoietic Innovative Therapies, Biomedical Innovation Unit, Centro de Investigaciones Energéticas, Medioambientales y Tecnologicas (CIEMAT), Madrid, Spain. ¹¹Advanced Therapies Unit, Instituto de Investigacion Sanitaria Fundacion Jiménez Díaz, Madrid, Spain. ¹²Centro de Investigación Biomédica en Red de Enfermedades Raras (CIBERER), Madrid, Spain. ¹³Flow Cytometry Core Unit, Biotechnology Programme, Spanish National Cancer Research Center (CNIO), Madrid, Spain. ¹⁴Bioinformatics Unit, Structural Biology Programme, Spanish National Cancer Research Center (CNIO), Madrid, Spain. ¹⁶Advanced Optical Microscopy – ISCIII Madrid, Madrid, Spain. ¹⁷Breast Cancer Clinical Research Unit, Centro Nacional de Investigaciones Oncológicas, Madrid, Spain. ¹⁸Medical Oncology, Hospital de Fuenlabrada, Madrid, Spain. ¹⁸Peinado@cnio.es